



ELSEVIER

Contents lists available at ScienceDirect

## Journal of the Mechanics and Physics of Solids

journal homepage: [www.elsevier.com/locate/jmps](http://www.elsevier.com/locate/jmps)

## The role of mechanics during brain development

Silvia Budday<sup>a</sup>, Paul Steinmann<sup>a</sup>, Ellen Kuhl<sup>b,\*</sup><sup>a</sup> Chair of Applied Mechanics, Department of Mechanical Engineering, University of Erlangen/Nuremberg, 91058 Erlangen, Germany<sup>b</sup> Departments of Mechanical Engineering, Bioengineering, and Cardiothoracic Surgery, Stanford University, 496 Lomita Mall, Stanford, CA 94305, USA

## ARTICLE INFO

## Article history:

Received 5 April 2014

Received in revised form

28 May 2014

Accepted 24 July 2014

Available online 9 August 2014

## Keywords:

Brain development

Cortical folding

Thin films

Growth

Instabilities

## ABSTRACT

Convolutions are a classical hallmark of most mammalian brains. Brain surface morphology is often associated with intelligence and closely correlated with neurological dysfunction. Yet, we know surprisingly little about the underlying mechanisms of cortical folding. Here we identify the role of the key anatomic players during the folding process: cortical thickness, stiffness, and growth. To establish estimates for the critical time, pressure, and the wavelength at the onset of folding, we derive an analytical model using the Föppl–von Kármán theory. Analytical modeling provides a quick first insight into the critical conditions at the onset of folding, yet it fails to predict the evolution of complex instability patterns in the post-critical regime. To predict realistic surface morphologies, we establish a computational model using the continuum theory of finite growth. Computational modeling not only confirms our analytical estimates, but is also capable of predicting the formation of complex surface morphologies with asymmetric patterns and secondary folds. Taken together, our analytical and computational models explain why larger mammalian brains tend to be more convoluted than smaller brains. Both models provide mechanistic interpretations of the classical malformations of lissencephaly and polymicrogyria. Understanding the process of cortical folding in the mammalian brain has direct implications on the diagnostics of neurological disorders including severe retardation, epilepsy, schizophrenia, and autism.

© 2014 The Authors. Published by Elsevier Ltd. This is an open access article under the CC BY license (<http://creativecommons.org/licenses/by/3.0/>).

## 1. Introduction

For more than a century, the unique surface morphology of the mammalian brain has fascinated scientists across all disciplines (Le Gros Clark, 1945): why does the brain have this complex convoluted structure, and, more importantly, to which extent is brain structure correlated with brain function (Welker, 1990)? From a mechanics point of view, these questions naturally translate into the quest for a basic understanding of brain morphology (Bayly et al., 2014): what are the underlying mechanisms of brain folding?

The mammalian brain is composed of an outer cortical layer of gray matter, consisting primarily of cell bodies, and an inner subcortical core of white matter, consisting primarily of axons. Within the limited space inside the skull, gyrification, the folding of the cortical layer, is viewed as a process to maximize the number of cell bodies and minimize the distance between them (Zilles et al., 2013). The total number of neurons, the number of connections, and the signaling speed are

\* Corresponding author. Tel.: +1 650 450 0855; fax: +1 650 725 1587.

E-mail addresses: [silvia.letttau@lth.uni-erlangen.de](mailto:silvia.letttau@lth.uni-erlangen.de) (S. Budday), [paul.steinmann@lth.uni-erlangen.de](mailto:paul.steinmann@lth.uni-erlangen.de) (P. Steinmann), [ekuhl@stanford.edu](mailto:ekuhl@stanford.edu) (E. Kuhl).

URL: <http://biomechanics.stanford.edu> (E. Kuhl).

directly correlated with the capacity of information processing. It is thus not surprising that not only the total brain volume, but also the brain surface area, is viewed as strong indicators of intelligence (Roth and Dicke, 2005). The ratio between brain surface area and brain volume, and with it the degree of gyrification, can vary significantly between species (Hofman, 1989). With 86 billion neurons, 0.15 quadrillion connections, and a mass of 1500 g, the human brain is often considered as the most developed mammalian brain (Herculano-Houzel, 2009).

Fig. 1 illustrates the average surface-to-volume relation of shrew, hedgehog, cat, monkey, human, and dolphin brains (Hofman, 1989). The graph confirms our intuition that larger mammals generally tend to have larger brains (Welker et al.). However, surprisingly, the surface area of the mammalian brain increases disproportionately faster than its volume (Roth and Dicke, 2005). In the log–log plot, the surface-to-volume ratio scales with a slope of 0.9, which is significantly larger than the slope of  $2/3$  for isometric scaling: larger mammals not only have larger, but also more convoluted brains. This naturally raises the question (Geschwind and Rakic, 2013): what is the evolutionary advantage of a folded brain?

Fig. 2 shows three explanted mammalian brains, which reconfirm that larger mammals tend to have larger brains (Sun and Hevner, 2014): the cow brain is larger than the pig brain, which in turn is larger than the brain of the sheep. Frontal coronal sections of the three brains illustrate that the degree of gyrification increases with brain size: the surface of the cow brain seems more folded than the surface of the pig brain, which seems more folded than the brain of the sheep (Zilles et al., 2013). The cortical thickness, however, seems to vary only marginally between the different species (Welker, 1990). Studies of mammalian brains indicate that brain size is not the only contributing factor to gyrification (Zilles et al., 1988). This motivates our hypothesis that rather than brain size, other anatomical features like cortical thickness, cortical stiffness, and cortical growth during brain development play a crucial role in pattern formation.

The development of the mammalian brain takes place in two distinct stages, which are crucial for cortical folding (Roth and Dicke, 2005): first, progenitor cells located around the ventricles divide symmetrically into two new progenitor cells to increase the total number of cells. Then, these newly created cells divide asymmetrically into a progenitor cell and a neuron (Sun and Hevner, 2014). Neurons migrate toward the surface along radial glial cells to form the cortical layer (Hatten, 1999). According to the radial unit hypothesis, all neurons of the same progenitor cell stack up on top of one another to form a cortical column (Rakic, 1988). Symmetric division is therefore primarily responsible for an increase in brain surface area, while asymmetric division is primarily responsible for an increase in cortical thickness (Roth and Dicke, 2005). Irregularities in cell division or cell migration can evoke abnormalities in surface area or thickness (Hatten, 1999). Those range from polymicrogyria, a malformation associated with an increased surface area and an excessive number of small folds (Tortori-Donati et al., 2005), to lissencephaly, a malformation associated with an increased cortical thickness and a reduced number of shallow folds (Landrieu et al., 1998). Severe malformations are often correlated with neurological disorders, including developmental delay, epilepsy, schizophrenia, and autism (Raybaud and Widjaja, 2011). Despite its pathophysiological importance, the phenomenon of cortical folding remains barely understood (Ronan et al., 2014).

Cytological studies alone fail to explain the process of cortical folding (Schwartzkroin and Walsh, 2000) and seem to indicate that mechanical factors could play a crucial role (Bayly et al., 2013). Two competing hypotheses suggest that cortical folding is either driven by axonal tension (Van Essen, 1997) or by differential growth (Richman et al., 1975). There is no direct evidence for either of these theories. Axonal tension, a mechanism to bring functionally related units topographically closer

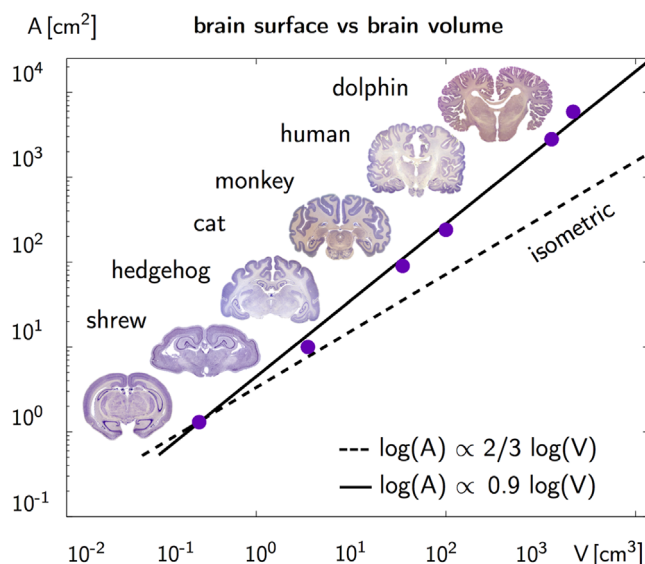
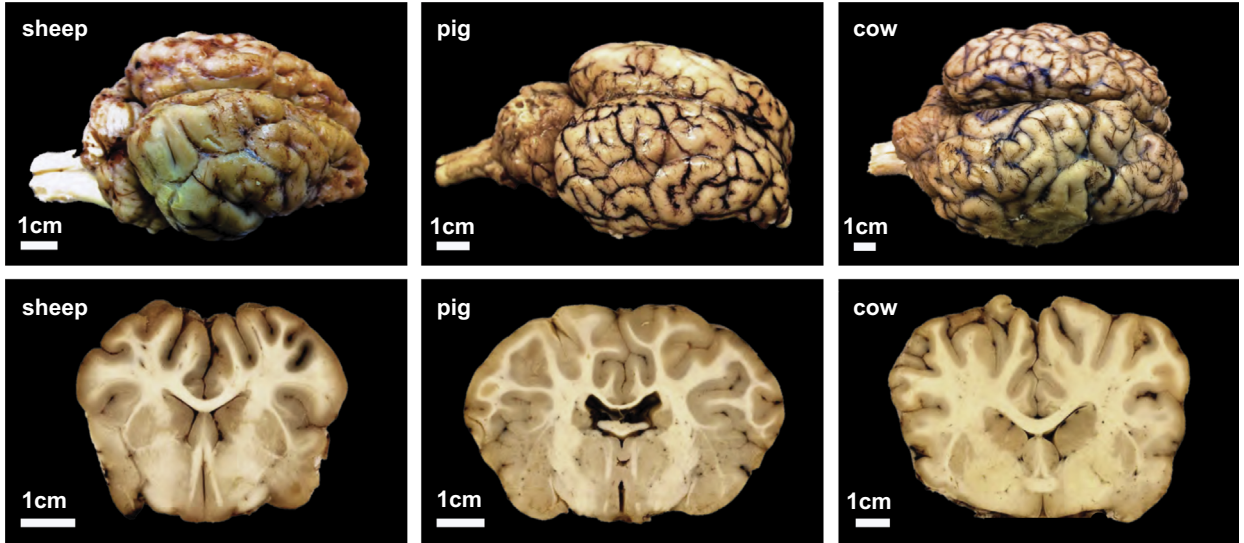


Fig. 1. Surface-to-volume ratio of the mammalian brain. Larger mammals have larger brains (Welker et al.). The dashed line with a slope of  $2/3$  indicates isometric scaling for which brain surface area would scale proportionally with brain volume. The solid line with a slope of 0.9 indicates that the mammalian brain surface area increases disproportionately faster than brain volume (Hofman, 1989). The degree of gyrification increases with brain size.



**Fig. 2.** Surface morphology of the mammalian brain. Larger mammals have larger brains: the cow brain, right, is larger than the pig brain, middle, which is larger than the sheep brain, left. Photographs of the entire brain, upper row, and a frontal coronal brain section, lower row, illustrate the characteristic folding pattern: the surface of the cow brain, right, is more folded than the surface of the pig brain, middle, which is more folded than the sheep brain, left. The degree of gyrification increases with brain size.

together, can explain folding irrespective of tissue stiffness, but disagrees with dissection experiments, which reveal significant tangential tension in the outer layers but not inside the developing gyri (Xu et al., 2010). Differential growth, a mechanism to release residual stresses by surface buckling, agrees well with dissection experiments, but relies on unrealistic stiffness differences between cortex and subcortex (Bayly et al., 2014). From other biological systems we know that differential growth is capable of generating sufficient compressive stresses to induce structural instabilities (Moulton and Goriely, 2011). Different geometric constraints, stiffness ratios, and growth rates may evoke different types of instabilities like buckles, wrinkles, creases, or folds (Li et al., 2012). Soft materials are especially susceptible to surface folding because of their low material stiffness (Li et al., 2011). Unfortunately, experiments to characterize the stiffness of the brain are rare and measured stiffness values span several orders of magnitude (Franceschini, 2006). Virtual experiments and systematic parameter studies provide a powerful alternative to explore the developing mammalian brain.

Here we model brain development using the continuum theory of finite growth (Rodriguez et al., 1994). We model the cortex as a morphogenetically growing outer layer of cell bodies and the subcortex as a strain-driven growing inner core of axons. Motivated by experiments of axon elongation (Bray, 1984), we assume that chronic axonal overstretch activates mechanotransduction pathways, which collectively result in a gradual increase in axonal length (Dennerll et al., 1989). This approach combines the two popular hypotheses of cortical folding, axonal tension and differential growth (Bayly et al., 2013). Using this model, we explore the effect of three key players on cortical folding: cortical thickness, stiffness, and growth. Since the absolute cortical stiffness and growth rate are poorly characterized (Franceschini et al., 2006), we explore the role of the relative cortical stiffness, and growth rate with respect to the subcortical properties.

The remainder of this paper is organized as follows: in Section 2, we present our analytical model for cortical folding to establish analytical estimates for the critical time, the critical pressure, and the critical wavelength at the onset of folding. In Section 3, we introduce our continuum model for finite growth to predict brain surface morphologies beyond the onset of folding. In Section 4, we summarize its computational solution within a nonlinear finite element setting. In Section 5, we utilize our model and perform systematic sensitivity studies of cortical thickness, stiffness and growth to understand the origin of pathological malformations. We close by a critical discussion of our results and their potential impact on understanding brain development in Section 6.

## 2. Analytical model

To establish analytical estimates for the brain surface morphology, we approximate cortical folding as the instability problem of a confined, layered medium subjected to growth-induced compression. We adopt the Föppl–von Kármán theory (Föppl, 1907; von Kármán, 1910), and model the cortical deflection  $w$  using the classical fourth order plate equation (Dervaux et al., 2009),

$$\frac{E_c}{1-\nu_c^2} \frac{t_c^3}{12} \frac{d^4 w}{dx^4} + P t_c \frac{d^2 w}{dx^2} = q. \quad (1)$$

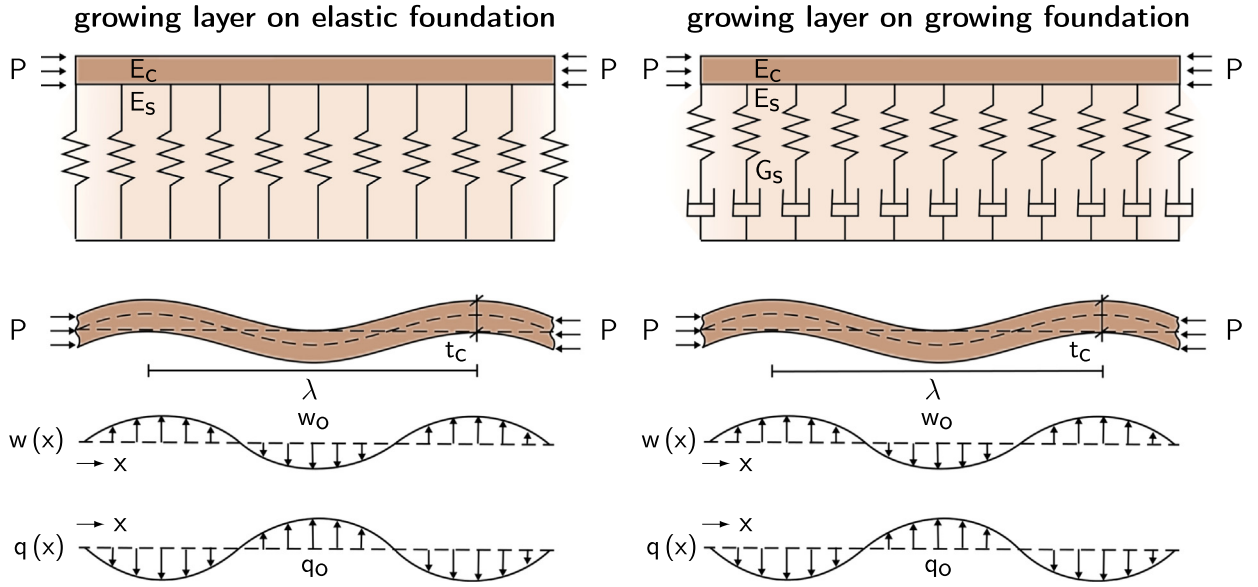


**Fig. 3.** Analytical model of confined, layered medium subjected to growth-induced compression. Growing layer on an elastic foundation, left, and on a growing foundation, right. We model cortical folding using the classical fourth order Föppl–von Kármán plate theory and adopt a sinusoidal ansatz for the deflection  $w$ , which generates a sinusoidal transverse force  $q$ . This provides analytical estimates for the critical cortical pressure  $P^{\text{crit}}$  and for the wavelength  $\lambda^{\text{crit}}$  parameterized in terms of the cortical thickness  $t_c$ , the cortical and subcortical Young's moduli  $E_c$  and  $E_s$ , and the cortical and subcortical growth rates  $G_c$  and  $G_s$ .

**Fig. 3** illustrates the analytical model with the cortical deflection  $w$ , Young's modulus of the cortex  $E_c$ , Poisson's ratio of the cortex  $\nu_c$ , the cortical thickness  $t_c$ , the cortical pressure  $P$ , and the deflection-induced transverse force of the subcortical foundation  $q$ . We adopt a sinusoidal ansatz for the cortical deflection,

$$w(x) = w_0 \cos(nx) \quad \text{with} \quad n = 2\pi/\lambda^{\text{crit}}, \quad (2)$$

where the amplitude  $w_0$  represents the sulcal depth, the wavenumber  $n$  represents the number of gyri and sulci, and the wavelength  $\lambda^{\text{crit}}$  represents the distance between two neighboring gyri. With this ansatz, the fourth order equation for cortical folding (1) takes the general form (Biot, 1957),

$$\frac{E_c}{1-\nu_c^2} \frac{t_c^3}{12} n^4 w_0 \cos(nx) - P t_c n^2 w_0 \cos(nx) = q(x), \quad (3)$$

where the transverse force  $q$  depends on the nature of the subcortical foundation. In the following, we illustrate analytical estimates for the critical pressure  $P^{\text{crit}}$  and the critical wavelength  $\lambda^{\text{crit}}$  for both an elastic foundation (Biot, 1937) as shown in **Fig. 3**, left, and a growing foundation (Biot, 1957) as shown in **Fig. 3**, right.

### 2.1. Growing cortex on elastic subcortex

To establish analytical estimates for cortical folding on an elastic subcortical foundation, we interpret the subcortex as an infinite half-space and impose a sinusoidal deflection  $w(x) = w_0 \cos(nx)$  with a wavelength  $n$  and an amplitude  $w_0$  on the upper boundary. This deflection evokes a transverse force  $q(x)$  with the same wavelength  $n$ ,

$$q(x) = q_0 \cos(nx) \quad \text{with} \quad q_0 = -\frac{E_s}{2[1-\nu_s^2]} n w_0. \quad (4)$$

Its amplitude  $q_0$  depends on the amplitude of the deflection  $w_0$ , and, through the analytical solution of the elastic half space in terms of the Airy stress function, on Young's modulus of the subcortex  $E_s$ , on Poisson's ratio of subcortex  $\nu_s$ , and on the wavenumber  $n$  (Biot, 1937). Inserting this ansatz (4) into the Föppl–von Kármán plate equation (3) yields the following equation for the cortical pressure  $P$ ,

$$P = \frac{1}{12} \frac{E_c}{1-\nu_c^2} t_c^2 n^2 + \frac{1}{2} \frac{E_s}{1-\nu_s^2} \frac{1}{t_c n}. \quad (5)$$

**Fig. 4** illustrates the growth-induced cortical pressure  $P$  as a function of the wavenumber  $n$  for varying cortical and subcortical stiffnesses. The minimum of each curve corresponds to the critical pressure  $P^{\text{crit}}$  at which folding occurs. The corresponding value of  $n$  is the critical wavenumber. The dotted line illustrates the critical pressure for varying wavenumbers.

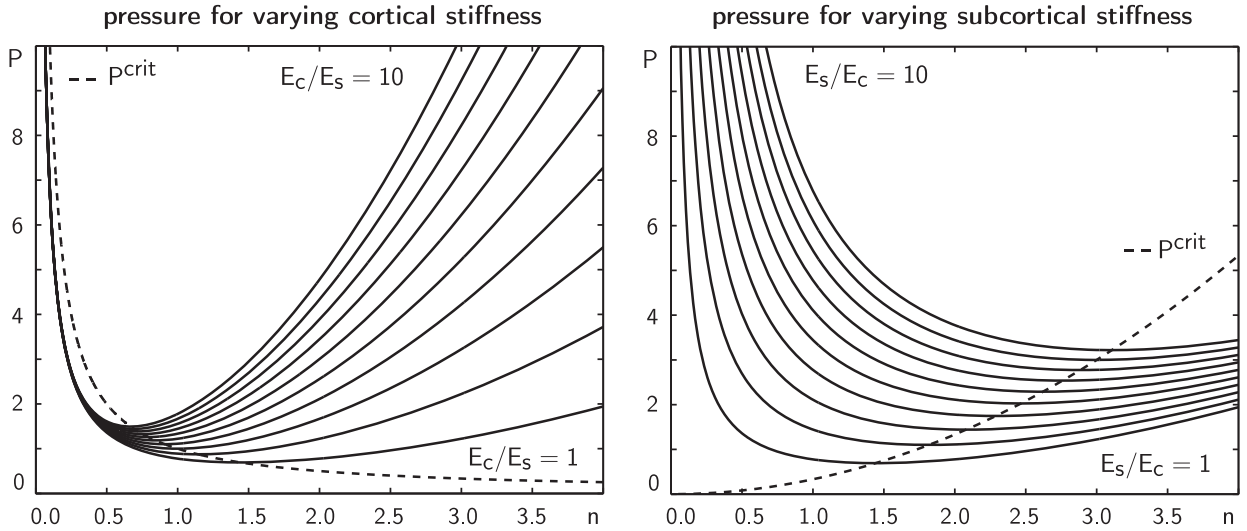


**Fig. 4.** Growth-induced cortical pressure  $P$  as a function of the wavenumber  $n$  for varying cortical stiffnesses  $E_c$ , left, and varying subcortical stiffnesses  $E_s$ , right. The dotted line characterizes the critical pressure  $P^{\text{crit}}$  at which folding occurs. The corresponding wavenumber  $n$  characterizes the critical folding pattern.

To determine the critical wavenumber  $n$ , we elaborate the minimization problem  $P(n) \rightarrow \min$ , or, equivalently,

$$\frac{dP}{dn} = \frac{1}{6} \frac{E_c}{1-\nu_c^2} t_c^2 n - \frac{1}{2} \frac{E_s}{1-\nu_s^2} \frac{1}{t_c n^2} = 0 \quad \text{thus } n = \frac{1}{t_c} \sqrt[3]{\frac{3(1-\nu_c^2)E_s}{1-\nu_s^2} E_c}. \quad (6)$$

We can then immediately obtain estimates for the critical pressure  $P^{\text{crit}}$  and the critical wavelength  $\lambda^{\text{crit}}$  as functions of the cortical thickness  $t_c$ , the cortical and subcortical Young's moduli  $E_c$  and  $E_s$ , and the cortical and subcortical Poisson's ratios  $\nu_c$  and  $\nu_s$  (Allen, 1969),

$$P^{\text{crit}} = \frac{3}{4} \frac{E_s}{1-\nu_s^2} \sqrt[3]{\frac{1-\nu_c^2}{3} \frac{E_c}{E_s}} \quad \text{and} \quad \lambda^{\text{crit}} = 2\pi t_c \sqrt[3]{\frac{1-\nu_s^2}{3} \frac{E_c}{E_s}}. \quad (7)$$

The Poisson's ratios of biological tissue are typically within the same range, i.e.,  $\nu_c \sim \nu_s$ . The most important observation is thus that the critical wavelength, the distance between two neighboring gyri, is directly proportional to the cortical thickness,  $\lambda^{\text{crit}} \propto t_c$ , and to the third root of the ratio of the cortical and subcortical stiffnesses,  $\lambda^{\text{crit}} \propto \sqrt[3]{E_c/E_s}$ .

**Remark 1** (*Special case of incompressibility*). If we assume that the cortex and subcortex are incompressible,  $\nu_c = 0.5$  and  $\nu_s = 0.5$ , the analytical estimates for the critical pressure and wavelength reduce to the following expressions,

$$P^{\text{crit}} = E_s \sqrt[3]{\frac{1}{3} \frac{E_c}{E_s}} \quad \text{and} \quad \lambda^{\text{crit}} = 2\pi t_c \sqrt[3]{\frac{1}{3} \frac{E_c}{E_s}}.$$

These are common estimates in materials sciences to characterize the buckling of a thin polymeric film on a thick polymeric substrate (Cao and Hutchinson, 2012): the wavelength of the buckling pattern is proportional to the thin film thickness,  $\lambda^{\text{crit}} \propto t_c$ , and to the third root of the ratio of the film-to-substrate stiffness,  $\lambda^{\text{crit}} \propto \sqrt[3]{E_c/E_s}$ .

## 2.2. Growing cortex on growing subcortex

To establish analytical estimates for cortical folding on a growing foundation, we again interpret the subcortex as an infinite half-space and impose a sinusoidal deflection  $w(x) = w_0 \cos(nx)$  on its upper boundary. Yet, now we assume that this deflection is the sum of an elastic subcortical deflection  $w_0^e$  and subcortical growth  $w_0^g$ , such that  $w_0 = w_0^e + w_0^g$ . Similarly, we can additively decompose the deflection rate  $\dot{w}_0$  into an elastic part  $\dot{w}_0^e$  and a growth part  $\dot{w}_0^g$  (Lubarda, 2004),

$$w_0 = w_0^e + w_0^g \quad \text{with } \dot{w}_0^e = -\frac{2[1-\nu_s^2]}{E_s n} \dot{q}_0 \quad \text{and} \quad \dot{w}_0^g = G_s w_0^e = -G_s \frac{2[1-\nu_s^2]}{E_s n} \dot{q}_0. \quad (8)$$

The elastic deflection,  $w_0^e = -2[1-\nu_s^2]/[E_s n]q_0$ , and its rate,  $\dot{w}_0^e = -2[1-\nu_s^2]/[E_s n]\dot{q}_0$ , follow from inverting the elastic half-space relation in Eq. (4). The growth deflection rate  $\dot{w}_0^g$  represents the growing subcortex. We assume that subcortical growth is stretch-induced, proportional to the elastic subcortical deflection  $w_0^e$ , scaled by the subcortical growth rate  $G_s$ . Combining all three equations yields an equation for the transverse force  $q_0$  as a Maxwell-type viscoelastic response to the

deflection  $w_0$ ,

$$\dot{q}_0 + G_s q_0 = -\frac{E_s}{2[1-\nu_s^2]} n \dot{w}_0. \quad (9)$$

We introduce a sinusoidal representation of the transverse force  $q(x)$  and adopt a convolution type solution for the amplitude  $q_0$ ,

$$q = q_0 \cos(nx) \quad \text{with} \quad q_0(t) = -\frac{E_s}{2[1-\nu_s^2]} n \int_{-\infty}^t \exp(-G_s[t-s]) \frac{dw_0}{ds} ds. \quad (10)$$

We choose an exponential ansatz for the deflection amplitude,  $w_0(t) = W_0 \exp(Gt)$ , such that  $dw_0/ds = Gw_0(t)$ , where  $G$  is the characteristic time constant of cortical folding. We insert Eq. (10) into the Föppl–von Kármán plate equation (3) to eventually obtain the equation for the cortical pressure,

$$P = \frac{1}{12} \frac{E_c}{1-\nu_c^2} t_c^2 n^2 + \frac{1}{2} \frac{E_s}{1-\nu_s^2} \frac{G}{G+G_s} \frac{1}{t_c n}. \quad (11)$$

Similar to the elastic foundation, we evaluate the minimization problem  $P(n) \rightarrow \min$  to determine the critical wavenumber  $n$ ,

$$\frac{dP}{dn} = \frac{1}{6} \frac{E_c}{1-\nu_c^2} t_c^2 n - \frac{1}{2} \frac{E_s}{1-\nu_s^2} \frac{G}{G+G_s} \frac{1}{t_c n^2} \stackrel{!}{=} 0 \rightarrow n = \frac{1}{t_c} \sqrt[3]{\frac{1-\nu_c^2}{1-\nu_s^2} \frac{E_s}{E_c} \frac{G}{G+G_s}}. \quad (12)$$

The estimates for the critical pressure  $P^{\text{crit}}$  and the wavelength  $\lambda^{\text{crit}}$  then follow immediately as functions of the cortical thickness  $t_c$ , the cortical and subcortical Young's moduli  $E_c$  and  $E_s$ , the cortical and subcortical Poisson's ratios  $\nu_c$  and  $\nu_s$ , the subcortical growth rate  $G_s$ , and the characteristic time constant of cortical folding  $G$ ,

$$P^{\text{crit}} = \frac{3}{4} \frac{E_s}{1-\nu_s^2} \frac{G}{G+G_s} \sqrt[3]{\frac{1-\nu_c^2}{1-\nu_s^2} \frac{E_c}{E_s} \frac{G+G_s}{G}} \quad \text{and} \quad \lambda^{\text{crit}} = 2\pi t_c \sqrt[3]{\frac{1-\nu_s^2}{1-\nu_c^2} \frac{E_c}{E_s} \frac{G}{G+G_s}}. \quad (13)$$

Again, we can assume that Poisson's ratios of the cortex and subcortex are of the same order,  $\nu_c \sim \nu_s$ . From the remaining parameters, we conclude that the critical wavelength, the distance between two neighboring gyri, is directly proportional to the cortical thickness,  $\lambda^{\text{crit}} \propto t_c$ , to the third root of the ratio of the cortical and subcortical stiffnesses,  $\lambda^{\text{crit}} \propto \sqrt[3]{E_c/E_s}$ , and to the subcortical growth rate,  $\lambda^{\text{crit}} \propto \sqrt[3]{(G+G_s)/G}$ . At the onset of folding, we assume that the growth-induced pressure in the cortical layer is equivalent to the elastic modulus of the cortex,  $E_c/[1-\nu_c^2]$ , multiplied by the amount of cortical growth. In the simplest case, we can represent cortical growth as the product of the cortical growth rate  $G_c$  and the critical folding time  $t^{\text{crit}}$  (Bayly et al., 2013),

$$P^{\text{crit}} = \frac{E_c}{1-\nu_c^2} G_c t^{\text{crit}}. \quad (14)$$

By combining the critical pressure  $P^{\text{crit}}$  at the onset of folding (13.1) with the cortical pressure generated by growth (14), we obtain a critical condition at the onset of folding, expressed in terms of the critical folding time  $t^{\text{crit}}$  and the characteristic time constant for cortical folding  $G$ .

$$\frac{E_c}{1-\nu_c^2} G_c t^{\text{crit}} \stackrel{!}{=} \frac{3}{4} \frac{E_s}{1-\nu_s^2} \frac{G}{G+G_s} \sqrt[3]{\frac{1-\nu_c^2}{1-\nu_s^2} \frac{E_c}{E_s} \frac{G+G_s}{G}} \quad (15)$$

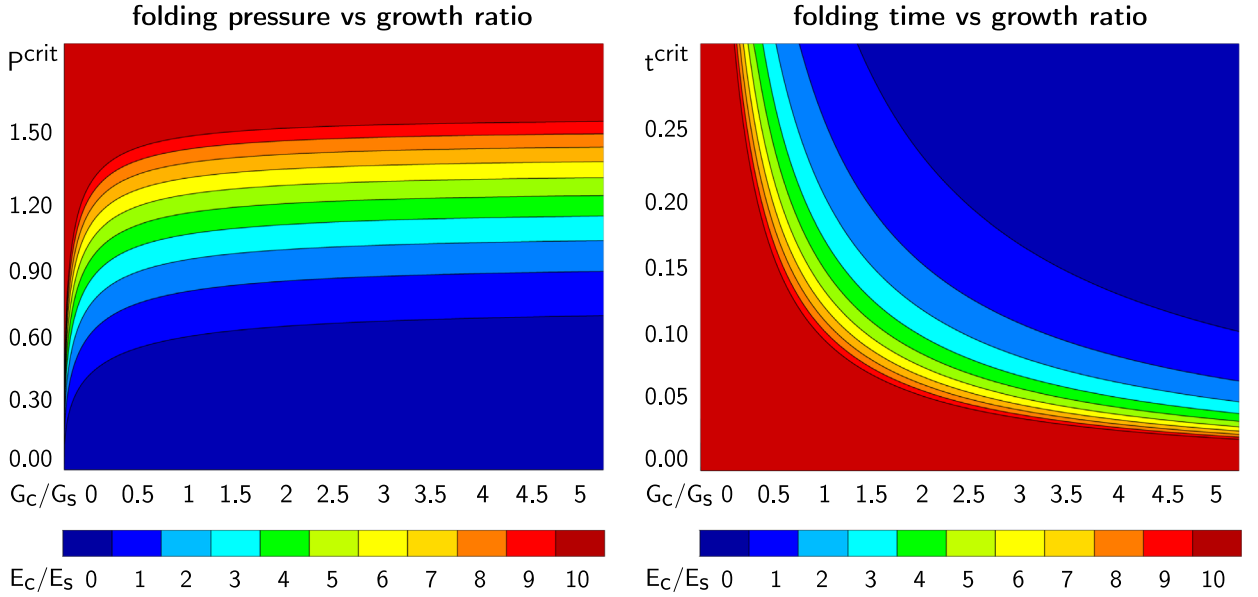
To further evaluate this condition, we choose  $G = 1/t^{\text{crit}}$  (Bayly et al., 2013), to obtain a quintic equation for the critical folding time,

$$(t^{\text{crit}})^5 + \frac{2}{G_s} (t^{\text{crit}})^4 + \frac{1}{G_s^2} (t^{\text{crit}})^3 - \frac{9}{64} \frac{[1-\nu_c^2]^2 E_s^2}{[1-\nu_s^2]^2 E_c^2} \frac{1}{G_s^3 G_s^2} \stackrel{!}{=} 0. \quad (16)$$

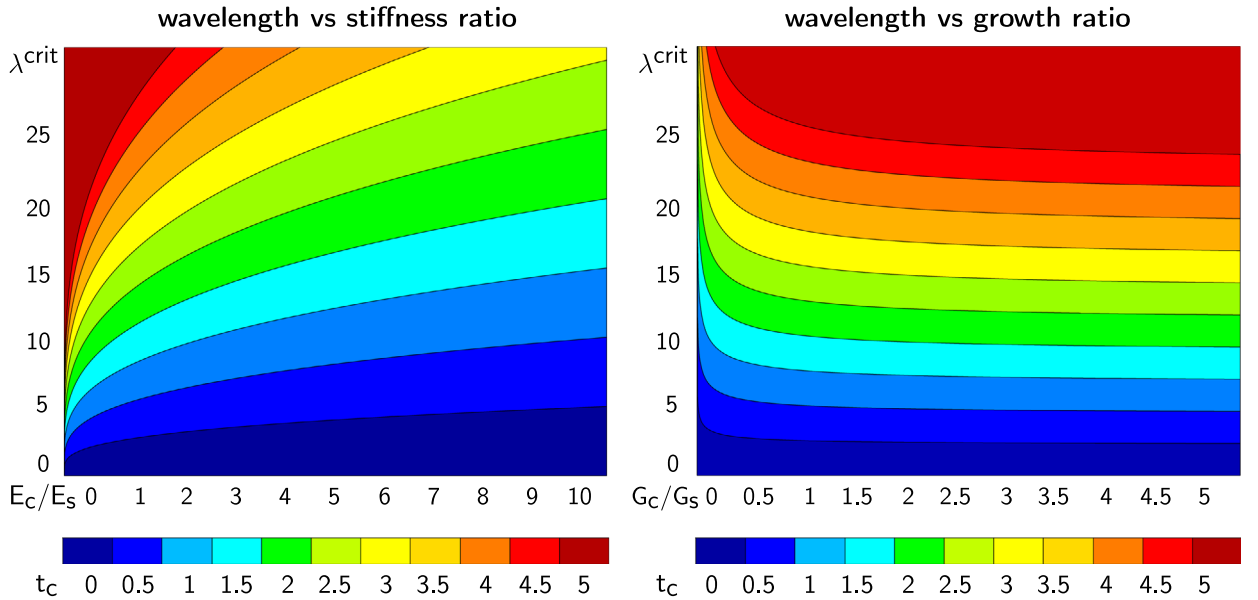
For given cortical and subcortical Young's moduli  $E_c$  and  $E_s$ , cortical and subcortical Poisson's ratios  $\nu_c$  and  $\nu_s$ , and cortical and subcortical growth rates  $G_c$  and  $G_s$ , we solve this equation for the folding time  $t^{\text{crit}}$  and then determine the critical pressure  $P^{\text{crit}}$  from Eq. (14) and the critical wavelength  $\lambda^{\text{crit}}$  from Eq. (13.2).

Fig. 5 illustrates the critical folding pressure  $P^{\text{crit}}$ , left, and the critical folding time  $t^{\text{crit}}$ , right, for varying growth ratios  $G_c/G_s$  and stiffness ratios  $E_c/E_s$ . For simplicity, we have assumed that cortex and subcortex have identical Poisson's ratios,  $\nu_c = \nu_s$ . The graphs agree with our intuition: the larger the cortical stiffness, the larger the required folding pressure  $P^{\text{crit}}$  and the smaller the folding time  $t^{\text{crit}}$ .

Fig. 6 illustrates the critical wavelength  $\lambda^{\text{crit}}$  for varying stiffness ratios  $E_c/E_s$  and varying cortical thicknesses  $t_c$ , left, and for varying growth ratios  $G_c/G_s$  and varying cortical thicknesses  $t_c$ , right. The graphs visualize our analytical estimates: the wavelength increases linearly with increasing cortical thickness  $t_c$ , increases with increasing stiffness ratio  $E_c/E_s$ , and decreases with increasing growth ratio  $G_c/G_s$ .



**Fig. 5.** Critical folding pressure  $p^{\text{crit}}$ , left, and critical folding time  $t^{\text{crit}}$ , right, for varying growth ratio  $G_c/G_s$  and varying stiffness ratio  $E_c/E_s$ . The folding pressure  $p^{\text{crit}}$  increases with increasing pressure  $p_c$  and increasing cortical stiffness  $E_c$ . The folding time  $t^{\text{crit}}$  decreases with increasing cortical growth  $G_c$  and increasing cortical stiffness  $E_c$ .



**Fig. 6.** Critical wavelength  $\lambda^{\text{crit}}$  for varying stiffness ratios  $E_c/E_s$  and varying cortical thicknesses  $t_c$ , left, and for varying growth ratios  $G_c/G_s$  and varying cortical thicknesses  $t_c$ , right. The wavelength  $\lambda^{\text{crit}}$  increases with increasing cortical stiffness  $E_c$ , with increasing subcortical growth rate  $G_s$ , and with increasing cortical thickness  $t_c$ .

**Remark 2 (Special case of incompressibility).** If we assume that the cortex and the subcortex are incompressible,  $\nu_c = 0.5$  and  $\nu_s = 0.5$ , the analytical estimates for the critical pressure and the wavelength reduce to the following expressions,

$$p^{\text{crit}} = E_s \frac{G}{G+G_s} \sqrt[3]{\frac{1}{3} \frac{E_c}{E_s} \frac{G+G_s}{G}} \quad \text{and} \quad \lambda^{\text{crit}} = 2\pi t_c \sqrt[3]{\frac{1}{3} \frac{E_c}{E_s} \frac{G+G_s}{G}}.$$

This simplification agrees with findings in the literature (Bayly et al., 2013): the wavelength of cortical folding is proportional to the cortical thickness,  $\lambda^{\text{crit}} \propto t_c$ , to the third root of the ratio of the cortical-to-subcortical stiffness,  $\lambda^{\text{crit}} \propto \sqrt[3]{E_c/E_s}$ , and to the subcortical growth rate  $\lambda^{\text{crit}} \propto \sqrt[3]{(G+G_s)/G} = \sqrt[3]{1+G_s} t^{\text{crit}}$ .

**Remark 3** (Special cases of solid- and fluid-like subcortex). As indicated in Fig. 3, we have modeled the growing subcortex as Maxwell type viscoelastic solid with  $\dot{q}_0 + G_s q_0 = -E_s/[2(1-\nu_s^2)]n\dot{w}_0$  in Eq. (9). This implies that the subcortex will behave solid-like and fluid-like in the two extreme cases,

$$G_s \ll G \quad \text{solid-like subcortex with } \lambda^{\text{crit}} = 2\pi t_c \sqrt[3]{\frac{1-\nu_s^2}{3} \frac{E_c}{1-\nu_c^2} \frac{E_s}{E_s}}$$

$$G_s \gg G \quad \text{fluid-like subcortex with } \lambda^{\text{crit}} \rightarrow \infty.$$

For small subcortical growth rates  $G_s \ll G$ , we immediately recover the solution for the elastic subcortex from Section 2.1. In Fig. 5, left and right, and Fig. 6, right, small subcortical growth rates correspond to large growth ratios  $G_c/G_s$ . We recover the special case of a solid-like subcortex as the asymptotic behavior for  $G_c/G_s \rightarrow \infty$ . Increasing the subcortical growth rate increases the wavelength  $\lambda^{\text{crit}}$ . For large enough subcortical growth rates  $G_s \gg G$ , we can suppress folding entirely. We recover the special case of a fluid-like subcortex as the asymptotic behavior for  $G_c/G_s \rightarrow 0$  with  $t^{\text{crit}} \rightarrow \infty$  and  $\lambda^{\text{crit}} \rightarrow \infty$ . These extreme cases agree with the literature of a wrinkling layer on a viscous substrate (Huang, 2005): the solid-like subcortex corresponds to the extreme case of a glassy substrate; the fluid-like subcortex corresponds to the extreme case of a rubbery substrate.

### 3. Continuum model

To explore the folding pattern beyond the onset of folding, we model growth using the nonlinear field theories of mechanics supplemented by the theory of finite growth. This results in a set of five equations, which define the kinematics, the constitutive behavior, the mechanical equilibrium, the growth kinematics, and the growth kinetics.

Fig. 7 illustrates our multiscale continuum model for cortical and subcortical growth in the developing mammalian brain. To characterize the kinematics of finite deformation, we introduce the deformation map  $\boldsymbol{\varphi}$ , which maps points  $\mathbf{X}$  from the undeformed configuration to their new positions  $\mathbf{x} = \boldsymbol{\varphi}(\mathbf{X}, t)$  in the deformed configuration. We then introduce the deformation gradient, which we decompose multiplicatively into an elastic part  $\mathbf{F}^e$  and a growth part  $\mathbf{F}^g$  (Garikipati, 2009),

$$\mathbf{F} = \nabla_{\mathbf{X}} \boldsymbol{\varphi} = \mathbf{F}^e \cdot \mathbf{F}^g \quad \text{and} \quad J = \det(\mathbf{F}) = J^e J^g. \quad (17)$$

A similar multiplicative decomposition holds for the Jacobian  $J$ , which we decompose into an elastic part  $J^e$  and a growth part  $J^g$ . To define the growth kinematics, for simplicity, we assume that growth is purely isotropic, parameterized in terms of a single scalar-valued growth multiplier  $\vartheta$ ,

$$\mathbf{F}^g = \vartheta \mathbf{I} \quad \text{and} \quad J^g = \det(\mathbf{F}^g) = \vartheta^3. \quad (18)$$

This implies that the grown volume  $J^g$  is identical to the growth multiplier cubed  $\vartheta^3$ . In the initial ungrown state, the growth multiplier is one,  $\vartheta = 1$ , such that  $\vartheta > 1$  and  $\vartheta < 1$  characterize volume growth and shrinkage. The elastic tensor  $\mathbf{F}^e$  and its Jacobian  $J^e$  then take the following explicit forms,

$$\mathbf{F}^e = \mathbf{F}/\vartheta \quad \text{and} \quad J^e = \det(\mathbf{F}^e) = J/\vartheta^3. \quad (19)$$

For simplicity, we assume that both cortex and subcortex are isotropic and elastic. We characterize their constitutive behavior through the following Neo-Hookean free energy parameterized exclusively in terms of the elastic tensor  $\mathbf{F}^e$  and its

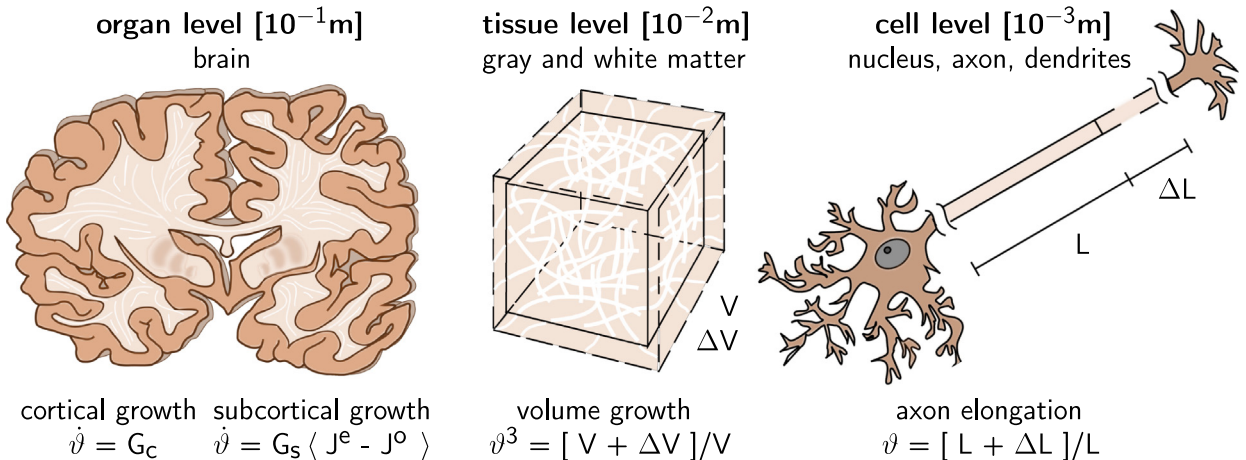


**Fig. 7.** Multiscale continuum model for cortical and subcortical growth. The cortex, the gray matter, grows morphogenetically at a constant rate  $G_c$ . Cortical growth induces subcortical deformation, which triggers subcortical growth. The subcortex, the white matter, grows at a stretch-dependent rate as  $G_s \langle J^e - J^0 \rangle$ , where  $G_s$  mimics the axon elongation rate and  $\langle J^e - J^0 \rangle$  activates growth only, if the elastic volume stretch  $J^e$  exceeds its baseline value  $J^0$ .

Jacobian  $J^e$ , for example as

$$\psi(\mathbf{F}^e) = \frac{1}{2}\lambda \ln^2(J^e) + \frac{1}{2}\mu[\mathbf{F}^e : \mathbf{F}^e - 3 - 2 \ln(J^e)], \quad (20)$$

where  $\lambda$  and  $\mu$  are the Lamé constants. This implies that only the elastic part of the deformation induces stress. For the following considerations, it proves convenient to reparameterize the free energy (20) in terms of the total deformation gradient  $\mathbf{F}$  and the growth factor  $\vartheta$ ,

$$\psi(\mathbf{F}, \vartheta) = \frac{1}{2}\lambda \ln^2\left(\frac{J}{\vartheta^3}\right) + \frac{1}{2}\mu\left[\frac{1}{\vartheta^2}\mathbf{F} : \mathbf{F} - 3 - 2 \ln\left(\frac{J}{\vartheta^3}\right)\right]. \quad (21)$$

Following standard arguments of thermodynamics, the Piola stress  $\mathbf{P}$  follows as energetically conjugate to the deformation gradient  $\mathbf{F}$ ,

$$\mathbf{P} = \frac{\partial\psi(\mathbf{F}, \vartheta)}{\partial\mathbf{F}} = \frac{1}{\vartheta^2}\mu\mathbf{F} + \left[\lambda \ln\left(\frac{J}{\vartheta^3}\right) - \mu\right]\mathbf{F}^{-t}. \quad (22)$$

The Piola stress enters the standard balance of linear momentum, the equation of mechanical equilibrium. In the absence of volume forces, the balance of linear momentum reduces to the vanishing divergence of the Piola stress,

$$\text{Div}(\mathbf{P}) = \mathbf{0}. \quad (23)$$

It remains to define the kinetics of growth, the equations that characterize the evolution of the growth multiplier in time (Menzel and Kuhl, 2012). Since the cortex consists primarily of cell nuclei whereas the subcortex consists primarily of axons, we assume different growth kinetics for the cortex and subcortex.

### 3.1. Cortical growth

For the cortex, we assume that growth is purely morphogenetic (BenAmar and Goriely, 2005), independent of mechanical stress or strain (Ambrosi and Mollica, 2002), characterized exclusively by the growth rate  $G_c$ ,

$$\dot{\vartheta} = G_c. \quad (24)$$

The cortical growth rate  $G_c$  may vary in time and space, depending on the current stage of development and on the regional location. For simplicity, here we let the cortex grow linearly in time and homogeneously in space,  $G_c = \text{const}$ .

### 3.2. Subcortical growth

For the subcortex, we assume that growth is stretch-induced (Kuhl, 2014). Cortical growth induces extreme deformations in the subcortex. The subcortex is primarily populated by axons, which lengthen gradually when subject to chronic stretch (Bray, 1984). We make the following ansatz,

$$\dot{\vartheta} = G_s \langle J^e - J^0 \rangle = G_s \langle J / \vartheta^3 - J^0 \rangle, \quad (25)$$

where  $G_s$  is the subcortical growth rate. With  $\langle J^e - J^0 \rangle = J^e - J^0$  for  $J^e > J^0$  and  $\langle J^e - J^0 \rangle = 0$  otherwise, the term in the Macaulay brackets activates growth only if the elastic volume stretch  $J^e$  exceeds its baseline value  $J^0$ , i.e., when axons are stretched beyond their physiological limit (Dennerll et al., 1989).

**Remark 4** (Stresses). To provide a more intuitive illustration of the Piola stress, we re-evaluate the thermodynamic stress definition  $\mathbf{P} = \partial\psi/\partial\mathbf{F}$  of Eq. (22), yet now, formulated in terms of the elastic deformation  $\mathbf{F}^e$ , using the Neo-Hookean free energy (20),

$$\mathbf{P} = \frac{\partial\psi(\mathbf{F}^e)}{\partial\mathbf{F}} = \frac{\partial\psi(\mathbf{F}^e)}{\partial\mathbf{F}^e} : \frac{\partial\mathbf{F}^e}{\partial\mathbf{F}} = \mathbf{P}^e \cdot \mathbf{F}^{g-t} = \frac{1}{\vartheta}\mathbf{P}^e. \quad (26)$$

This indicates that the Piola stress in Eq. (22) is nothing but the growth-weighted classic elastic Piola stress,

$$\mathbf{P}^e = \frac{d\psi(\mathbf{F}^e)}{d\mathbf{F}^e} = \mu\mathbf{F}^e + [\lambda \ln(J^e) - \mu]\mathbf{F}^{e-t}. \quad (27)$$

For the special case of isotropic growth, growth-weighting simplifies to dividing the elastic Piola stress by the growth factor  $\vartheta$ .

## 4. Computational model

To solve the nonlinear equations for brain development, we adopt a finite element discretization in space and a finite difference discretization in time. We introduce the growth multiplier  $\vartheta$  as an internal variable, and solve its evolution equation for cortical growth (24) and subcortical growth (25) locally at the integration point level. We approximate the growth rate  $\dot{\vartheta}$  through a finite difference ansatz,

$$\dot{\vartheta} = [\vartheta - \vartheta_n]/\Delta t, \quad (28)$$

where  $\vartheta$  is the current growth multiplier,  $\vartheta_n$  is the growth multiplier of the previous time step, and  $\Delta t = t - t_n$  denotes the current time increment.

#### 4.1. Cortical growth

For the cortex, we determine the new growth multiplier  $\vartheta$  explicitly through a linear update of the previous growth multiplier  $\vartheta_n$  using Eqs. (24) and (28) as

$$\vartheta = \vartheta_n + G_c \Delta t. \quad (29)$$

To solve the global set of equations, we determine the tangent moduli of the cortex through the total derivative of the Piola stress  $\mathbf{P}$  from Eq. (22) with respect to the deformation gradient  $\mathbf{F}$  and fix the current growth multiplier  $\vartheta$ ,

$$\mathbf{A} = \frac{d\mathbf{P}}{d\mathbf{F}} = \frac{\partial \mathbf{P}}{\partial \mathbf{F}} \Big|_{\vartheta} = \mathbf{A}^e. \quad (30)$$

Since the growth multiplier is independent of the current deformation, the tangent moduli simply consist of the growth-weighted classical elastic tangent moduli (Papastavrou et al., 2013),

$$\mathbf{A}^e = \frac{1}{\vartheta^2} \mu \mathbf{I} \otimes \mathbf{I} + \left[ \mu - \lambda \ln \left( \frac{J}{\vartheta^3} \right) \right] \mathbf{F}^{-t} \underline{\otimes} \mathbf{F}^{-1} + \lambda \mathbf{F}^{-t} \otimes \mathbf{F}^{-t}. \quad (31)$$

Here, we have used the following abbreviations,  $\{\bullet \overline{\otimes} \circ\}_{ijkl} = \{\bullet\}_{ik} \{\circ\}_{jl}$  and  $\{\bullet \underline{\otimes} \circ\}_{ijkl} = \{\bullet\}_{il} \{\circ\}_{jk}$ , for the non-standard fourth order products.

#### 4.2. Subcortical growth

For the subcortex, we apply an implicit time integration scheme and reformulate the evolution equation (25) with the help of the finite difference ansatz (28). This introduces the discrete residual  $R$  in terms of the unknown growth multiplier  $\vartheta$ ,

$$R = \vartheta - \vartheta_n - G_s \left\langle \frac{1}{\vartheta^3} J - J^0 \right\rangle \Delta t \doteq 0. \quad (32)$$

To solve this nonlinear equation, we adopt a local Newton iteration. For each iteration step, we calculate the linearization of the residual  $R$  with respect to the current growth multiplier  $\vartheta$ ,

$$K = \frac{dR}{d\vartheta} = 1 + 3G_s \frac{1}{\vartheta^4} J \Delta t \mathcal{H} \left( \frac{J}{\vartheta^3} - J^0 \right). \quad (33)$$

The Heaviside step function  $\mathcal{H}$  is one during growth,  $J/\vartheta^3 - J^0 > 0$ , and zero otherwise. Within each iteration step, we update the unknown growth multiplier,

$$\vartheta \leftarrow \vartheta - R/K, \quad (34)$$

until we achieve local convergence, i.e., until the absolute value of the growth update  $|R/K|$  is smaller than a user-defined convergence threshold. To solve the global set of equations, we determine the tangent moduli of the subcortex through the total derivative of the Piola stress  $\mathbf{P}$  from Eq. (22) with respect to the deformation gradient  $\mathbf{F}$ ,

$$\mathbf{A} = \frac{d\mathbf{P}}{d\mathbf{F}} = \frac{\partial \mathbf{P}}{\partial \mathbf{F}} \Big|_{\vartheta} + \frac{\partial \mathbf{P}}{\partial \vartheta} \otimes \frac{\partial \vartheta}{\partial \mathbf{F}} \Big|_{\mathbf{F}} = \mathbf{A}^e + \mathbf{A}^g. \quad (35)$$

The first term, the Hessian of the free energy function for constant growth,  $\vartheta = \text{const.}$ , defines the growth-weighted classical elastic tangent moduli similar to the case of cortical growth (31),

$$\mathbf{A}^e = \frac{\partial \mathbf{P}}{\partial \mathbf{F}} = \frac{1}{\vartheta^2} \mu \mathbf{I} \otimes \mathbf{I} + \left[ \mu - \lambda \ln \left( \frac{J}{\vartheta^3} \right) \right] \mathbf{F}^{-t} \underline{\otimes} \mathbf{F}^{-1} + \lambda \mathbf{F}^{-t} \otimes \mathbf{F}^{-t}. \quad (36)$$

The second term is specific to the constitutive equation (20) and characterizes the sensitivity of the Piola stress  $\mathbf{P}$  with respect to the growth multiplier  $\vartheta$ ,

$$\frac{\partial \mathbf{P}}{\partial \vartheta} = -\frac{1}{\vartheta^3} [2\mu \mathbf{F} + \lambda \mathbf{F}^{-t}]. \quad (37)$$

The third term is specific to both the kinetic equation for growth (25) and its algorithmic solution (33),

$$\frac{\partial \vartheta}{\partial \mathbf{F}} = \frac{\partial \vartheta}{\partial \vartheta} \frac{\partial \vartheta}{\partial \mathbf{F}} = \frac{1}{\vartheta^3} \frac{G_s \Delta t}{K} J \mathbf{F}^{-t}, \quad (38)$$

where  $\partial \vartheta / \partial \vartheta = K$  and  $\partial \vartheta / \partial \mathbf{F} = G_s J \mathbf{F}^{-t} / \vartheta^3$ . The Hessian of the free energy function for constant deformation,  $\mathbf{F} = \text{const.}$ ,

defines the correction of the constitutive moduli due to growth,

$$\mathbf{A}^g = -\frac{1}{\vartheta^6} \frac{G_s \Delta t}{K} J [2\mu \mathbf{F} + \lambda \mathbf{F}^{-t}] \otimes \mathbf{F}^{-t}. \quad (39)$$

The fourth-order tangent moduli for the cortex (30) and for the subcortex (35) enter the iteration matrix for the global Newton iteration. Upon convergence of the global Newton iteration, we store the current growth multiplier  $\vartheta$  locally at the integration point level.

**Remark 5** (*Tangent moduli*). Again, we can reformulate the definition of the elastic tangent operator  $\mathbf{A}^e = \partial \mathbf{P} / \partial \mathbf{F}$  in terms of the elastic deformation  $\mathbf{F}^e$  to obtain a more intuitive interpretation of its terms,

$$\mathbf{A}^e(\mathbf{F}^e) = \frac{\partial \mathbf{P}(\mathbf{F}^e)}{\partial \mathbf{F}} = \frac{\partial \mathbf{P}(\mathbf{F}^e)}{\partial \mathbf{F}^e} : \frac{\partial \mathbf{F}^e}{\partial \mathbf{F}} = [\mathbf{I} \otimes \mathbf{F}^{g-1}] : \frac{d\mathbf{P}(\mathbf{F}^e)}{d\mathbf{F}^e} : [\mathbf{I} \otimes \mathbf{F}^{g-t}] = \frac{1}{\vartheta^2} \frac{d\mathbf{P}^e(\mathbf{F}^e)}{d\mathbf{F}^e}. \quad (40)$$

This indicates that the elastic tangents in (31) and (36) are nothing but the growth-weighted standard tangent operator,

$$\frac{d\mathbf{P}^e(\mathbf{F}^e)}{d\mathbf{F}^e} = \frac{d^2\psi(\mathbf{F}^e)}{d\mathbf{F}^e \otimes d\mathbf{F}^e} = \mu \mathbf{I} \otimes \mathbf{I} + [\mu - \lambda \ln(J^e)] \mathbf{F}^{e-t} \otimes \mathbf{F}^{e-1} + \lambda \mathbf{F}^{e-t} \otimes \mathbf{F}^{e-t}. \quad (41)$$

For the special case of isotropic growth, this growth-weighting simplifies to dividing the tangent by the growth factor squared  $\vartheta^2$ .

## 5. Results

To illustrate the features of our computational model, we expand the analytical study in Section 2 beyond the onset of folding, which is difficult to assess analytically and has only been addressed recently by a few groups (Audoly and Boudaoud, 2008; Cao and Hutchinson, 2012). During brain development, constrained growth of the cortical layer induces compressive stresses  $\mathbf{P}$ . Once these stresses reach a critical value  $\mathbf{P}^{\text{crit}}$ , the brain surface buckles into a wavy pattern to partially release the growth-induced stress. In analogous to the analytical estimates in Section 2 and Fig. 6, we explore the role of the three main contributors to the folding pattern: the cortical thickness  $t_c$ , the stiffness ratio between cortex and subcortex  $E_c/E_s$ , and the growth ratio between cortex and subcortex  $G_c/G_s$ .

### 5.1. Sensitivity of surface morphology with respect to cortical thickness

To explore the effect of the initial cortical thickness  $t_c$  on the folding pattern, we explore constrained growth in a regular rectangular slice of  $2 \times 1 \times 0.05 \text{ cm}^3$  of a transverse brain section. We discretize the slice with  $80 \times 40 \times 1 = 3200$  tri-linear Q1 elements and 19,926 degrees of freedom and assume a plane strain state. To constrain growth, we fix the left, bottom, and right boundary nodes orthogonal to the boundary, but allow them to slide freely along the edge. We model the cortex as Neo Hookean elastic with Lamé constants  $\lambda_c = 34.2 \text{ kPa}$  and  $\mu_c = 3.3 \text{ kPa}$  (Soza et al., 2005) and assume that the subcortex is three times softer with  $\lambda_s = 11.4 \text{ kPa}$  and  $\mu_s = 1.1 \text{ kPa}$  (Budday et al., 2014). We fix the cortical growth rate to  $G_c = 2.0$ , the subcortical growth rate to  $G_s = 0.003$ , and the physiological limit for axonal growth to  $J^0 = 1.0$  (Chada et al., 1997). Since a perfectly regular rectangular domain would not fold in the computational simulation, we trigger an initial imperfection by selectively increasing the subcortical growth rate  $G_s$  by 10% in a  $0.05 \text{ cm}$  thin vertical band in the center of the rectangle (Bayly et al., 2013). We gradually increase the initial cortical thickness from  $t_{\text{crit}} = 0.125 \text{ mm}$  to  $t_{\text{crit}} = 1.000 \text{ mm}$  in eight equal steps of  $\Delta t_{\text{crit}} = 0.125 \text{ mm}$ .

Fig. 8 illustrates the sensitivity of the wavelength  $\lambda^{\text{crit}}$  with respect to the initial cortical thickness  $t_c$ . The eight dots indicate the computationally predicted wavelengths for the eight different cortical thicknesses. The eight figures inside the graph additionally illustrate the corresponding folding patterns. Simulations with coarser and finer meshes and with smaller and larger perturbations predicted similar folding patterns and similar wavelengths. This indicates that the computationally predicted surface morphology is relatively insensitive to the underlying discretization and to the imposed mode of perturbation. The dashed line shows the analytical wavelength-thickness relation for a growing cortical layer on a growing subcortical foundation according to Section 2. According to Eq. (8), the analytical solution is based on the additive decomposition of the rate of deformation into elastic and growth parts. It follows from evaluating equation (13), the equation to estimate the critical wavelength,  $\lambda^{\text{crit}} = 2\pi t_c \sqrt[3]{1 + G_s/G_c}$ , as a function of the characteristic time scale of folding  $G$ , which we obtain from iteratively solving the quintic equation (16) as  $G^5 - 64G_c^3[G_s + G]^2 = 0$ . The solid line shows the averaged computational wavelength-thickness relation for a morphogenetically growing cortex on a stretch-driven growing subcortex according to Sections 3 and 4. According to Eq. (17), the computational prediction is based on the multiplicative decomposition of the deformation gradient into elastic and growth parts. Fig. 8 suggests that the analytical estimate with the additive decomposition and the computational prediction with the multiplicative decomposition agree well in the small deformation limit (Li et al., 2011; Lubarda, 2004). Their direct comparison confirms that the wavelength increases linearly with the initial cortical thickness,  $\lambda^{\text{crit}} \propto t_c$ . The slope of  $m=10.20$  of the computational model is slightly higher than the slope of  $m=8.92$  of the analytical model, which indicates that the computational prediction is slightly stiffer than the

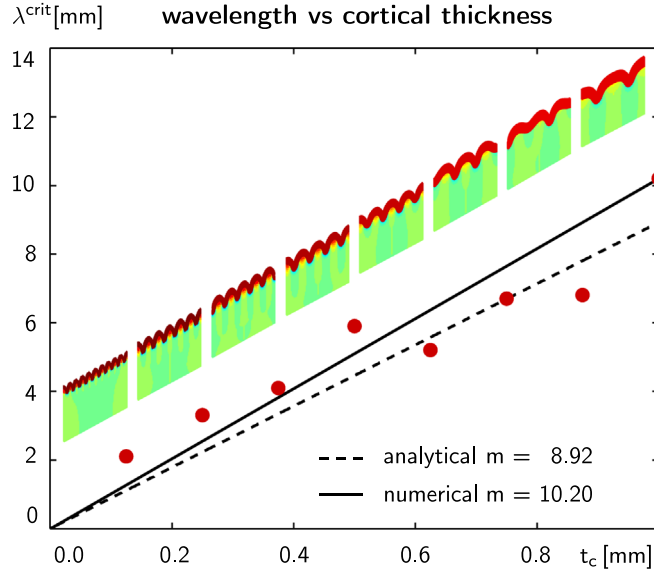


**Fig. 8.** Sensitivity of surface morphology with respect to initial cortical thickness for constrained growth in a rectangular domain. The dots illustrate the computationally predicted wavelengths  $\lambda^{\text{crit}}$  for varying cortical thicknesses  $t_c$ . The solid line shows the averaged computational wavelength–thickness relation for a morphogenetically growing cortex on a stretch-driven growing subcortex. The dashed line shows the analytical wavelength–thickness relation for a growing cortical layer on a growing subcortical foundation.

analytical estimate. This discrepancy is in agreement with the well-known overly stiff response of tri-linear finite elements, in particular in bending-dominated problems. In addition, the chosen homogeneous Neumann boundary conditions at the lateral sides enforce symmetric folding patterns for which the computationally predicted wavenumbers are always multiples of one half. Aside from these limitations, the analytically and computationally predicted surface morphologies are in excellent quantitative and qualitative agreement. Yet, additional discrepancies might arise between the wavelength-to-thickness relation on initially flat geometries as studied here and initially curved geometries (Li et al., 2011) of real mammalian brains.

## 5.2. Sensitivity of surface morphology with respect to stiffness ratio

To explore the effect of the stiffness ratio  $E_c/E_s$  on the folding pattern, we simulate growth of an elliptic brain slice to mimic an idealized transverse brain section during early development. While the cortical thickness  $t_c$  is a parameter that is easy to measure experimentally, the cortical and subcortical stiffnesses  $E_c$  and  $E_s$  are relatively difficult to determine. On one hand, in vivo experiments on living brain tissue seem virtually impossible. On the other hand, it remains questionable to which extent ex vivo experiments can provide useful estimates for the material properties of the living brain in vivo. Some effort has been made to identify the elastic material parameters of the human brain (Franceschini et al., 2006), yet, the reported values deviate considerably: Young's modulus was found to vary four orders of magnitude, from 0.5 kPa to 500 kPa, and even Poisson's ratio was reported to range from 0.2 to 0.5 (Franceschini, 2006). Due to the structural difference between neuronal cell bodies and neuronal axons, it seems reasonable to assume that the stiffness is not even uniform across the brain, and that cortical and subcortical stiffnesses are inherently different.

Although there is no general agreement of the absolute stiffness values of cortex and subcortex, we can still perform a sensitivity study of the cortical-to-subcortical stiffness ratio  $E_c/E_s$ . To this end, we simulate growth of an elliptic brain slice of an area of 4 cm<sup>2</sup>, an ellipticity ratio of 1.15, and a thickness of 0.005 cm. We discretize the ellipse with 3328 tri-linear Q1 elements and 20,358 degrees of freedom and assume a plane strain state. This discretization introduces 128 nodes on the outer boundary, which implies that it can capture a folding pattern with 16-folds at a resolution of eight nodes per wavelength. We model the cortex as Neo Hookean elastic with Lamé constants  $\lambda_c = 34.2$  kPa and  $\mu_c = 3.3$  kPa and systematically double the cortical-to-subcortical stiffness ratio  $E_c/E_s$  from  $2^2$  to  $2^5$  in four subsequent steps by adjusting the subcortical Lamé constants  $\lambda_s$  and  $\mu_s$ . We fix the cortical growth rate to  $G_c = 2.0$ , the subcortical growth rate to  $G_s = 0.003$ , and the physiological limit for axonal growth to  $J^0 = 1.0$  (Chada et al., 1997). In addition, we gradually vary the initial cortical thickness from  $t_{\text{crit}} = 0.25$  mm to  $t_{\text{crit}} = 1.00$  mm in four equal steps of  $\Delta t_{\text{crit}} = 0.25$  mm. In contrast to the perfectly regular rectangular domain, the elliptic domain possesses an inherent imperfection because of its varying curvature, and we do not need to impose additional artificial imperfections to trigger folding.

Fig. 9 illustrates the sensitivity of the wavelength  $\lambda^{\text{crit}}$  with respect to the initial cortical thickness  $t_c$  and the stiffness ratio  $E_c/E_s$ . Snapshots of each column have the same stiffness ratio  $E_c/E_s$  and are displayed at the same stage of cortical growth  $\vartheta$ , the stage of first self-contact within the corresponding column. Snapshots of each row have the same cortical thickness  $t_c$

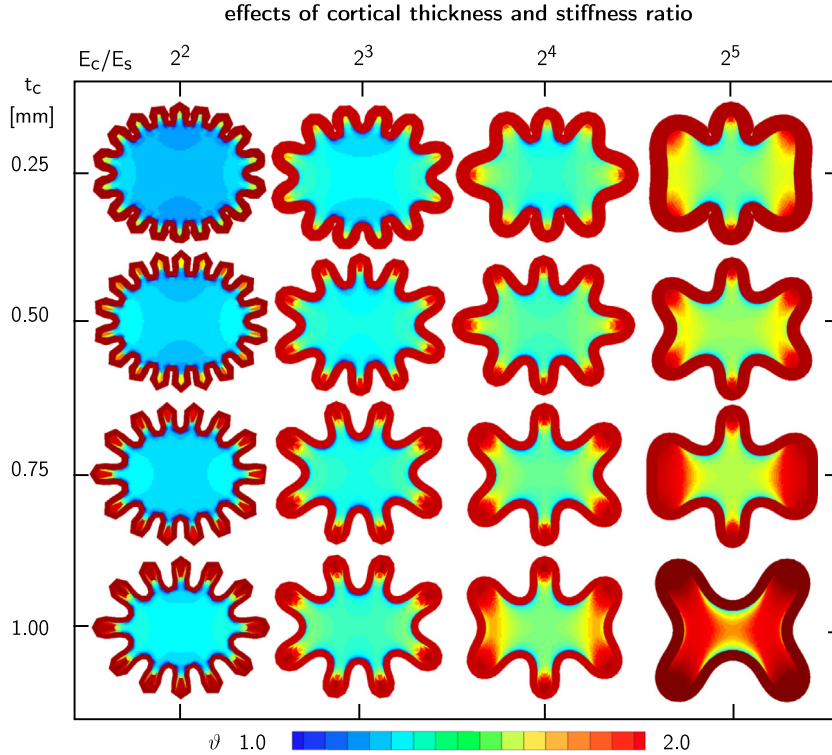


**Fig. 9.** Sensitivity of surface morphology with respect to initial cortical thickness and stiffness ratio for elliptic geometry. The wavelength  $\lambda^{\text{crit}}$  increases with increasing cortical thickness  $t_c$ , from top to bottom, and with increasing stiffness ratio,  $E_c/E_s$ , from left to right. Larger wavelengths induce larger subcortical stretch resulting in larger subcortical growth.

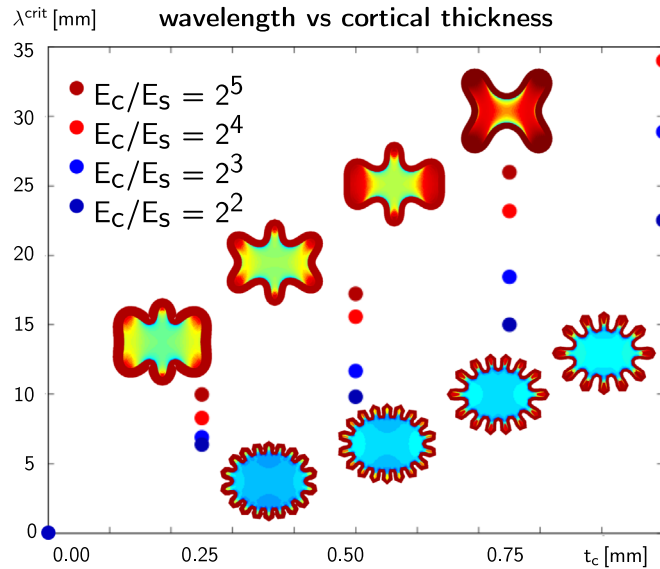
and are displayed for subsequent stages with increasing cortical growth  $\vartheta$  as the stiffness ratio increases. The computational simulation agrees well with the analytical estimates in Section 2: the wavelength  $\lambda^{\text{crit}}$  increases with increasing cortical thickness  $t_c$ , from top to bottom, and with increasing stiffness ratio,  $E_c/E_s$ , from left to right. In all cases, folding started first in the region of lowest curvature, on the shorter symmetry axis, and gradually propagated outwards to the regions of highest curvature. While cortical growth is identical in all 16 cases, and homogeneously distributed across the entire cortex, subcortical growth varies significantly across the 16 simulations and displays pronounced regional heterogeneities. In general, larger cortical wavelengths induce larger subcortical stretch resulting in larger subcortical growth. As the wavelength increases, the individual folds become deeper. As a consequence, subcortical growth is largest in the gyri and smallest in the sulci.

Fig. 10 summarizes the computationally predicted average wavelength  $\lambda^{\text{crit}}$ , i.e., the elliptical circumference divided by the number of folds  $n$ , for the four varying cortical thicknesses and the four varying stiffness ratios. In agreement with the analytical estimates in Section 2, the average wavelength increases linearly with increasing cortical thickness  $t_c$ , from left to right. Also in agreement with the analytical estimates, the average wavelength increases with increasing stiffness ratio  $E_c/E_s$ , from lower blue dots to upper red dots.

### 5.3. Sensitivity of surface morphology with respect to growth ratio

To explore the effect of the growth ratio  $G_c/G_s$  on the folding pattern, we simulate the same idealized elliptic transverse brain section as in Section 5.2 with an elliptic area of 4 cm<sup>2</sup>, an ellipticity ratio of 1.15, and a thickness of 0.005 cm. Again, we discretize the ellipse with 3328 tri-linear Q1 elements and 20,358 degrees of freedom and assume a plane strain state. We model the cortex as Neo Hookean elastic with Lamé constants  $\lambda_c = 34.2$  kPa and  $\mu_c = 3.3$  kPa (Soza et al., 2005) and assume that the subcortex is three times softer with  $\lambda_s = 11.4$  kPa and  $\mu_s = 1.1$  kPa (Budday et al., 2014). We fix the subcortical growth rate to  $G_s = 0.003$  and fix the physiological limit for axonal growth to  $J^0 = 1.0$ . We systematically increase the cortical-to-subcortical growth ratio  $G_c/G_s$  from  $10^{-1}$  via  $10^0$  and  $10^1$  to  $10^2$ . Similar to the previous example, we also vary the initial cortical thickness from  $t_{\text{crit}} = 0.25$  mm to  $t_{\text{crit}} = 1.00$  mm in four equal steps of  $\Delta t_{\text{crit}} = 0.25$  mm.

Fig. 11 illustrates the sensitivity of the wavelength  $\lambda^{\text{crit}}$  with respect to the initial cortical thickness  $t_c$  and the growth ratio  $G_c/G_s$ . All snapshots correspond to the stage of cortical growth, at which the final folding pattern of all 16 ellipses had fully developed. Again, folding started first in the region of lowest curvature, on the shorter symmetry axis, and gradually propagated outwards to the regions of highest curvature. Cortical growth is identical in all 16 cases and homogeneously distributed across each slice, whereas subcortical growth varies significantly across the 16 simulations and displays



**Fig. 10.** Sensitivity of surface morphology with respect to initial cortical thickness and stiffness ratio for elliptic geometry. The dots illustrate the computationally predicted average wavelengths  $\lambda^{\text{crit}}$  for varying cortical thicknesses  $t_c$  and varying stiffness ratios  $E_c/E_s$ . The average wavelength increases with increasing cortical thickness  $t_c$ , from left to right, and with increasing stiffness ratio,  $E_c/E_s$ , from lower blue dots to upper red dots. (For interpretation of the references to color in this figure caption, the reader is referred to the web version of this paper.)

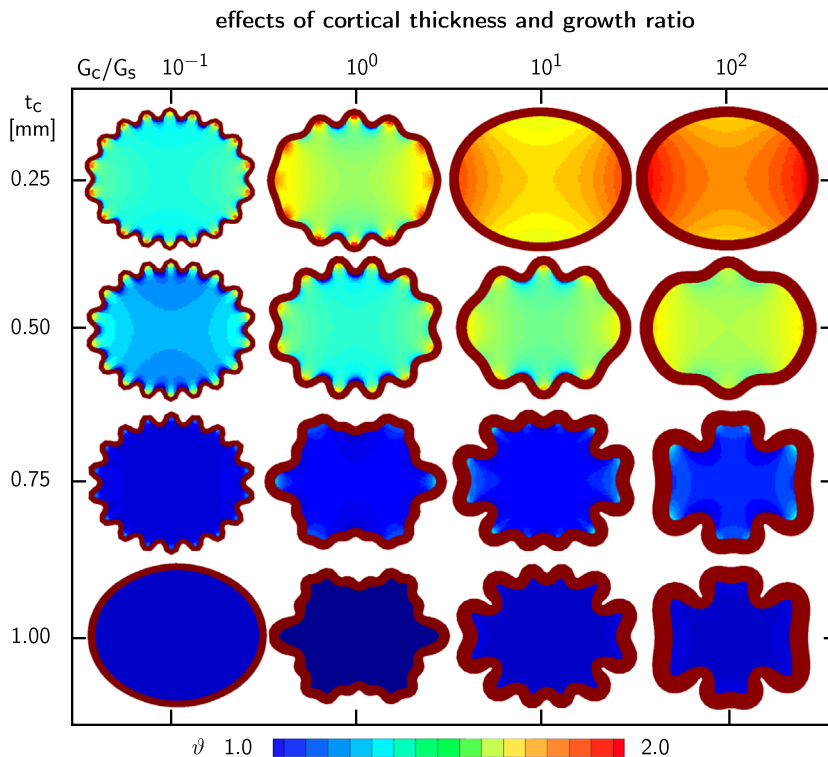


**Fig. 11.** Sensitivity of surface morphology with respect to initial cortical thickness and growth ratio for elliptic geometry. The wavelength of primary folding  $\lambda^{\text{crit}}$  increases with increasing cortical thickness  $t_c$ , from top to bottom. The overall wavelength increases with increasing growth ratios  $G_c/G_s$ , from left to right.

pronounced regional heterogeneities. The left column indicates that slow cortical growth rates  $G_c$  allow for balanced cortical and subcortical growth, which keeps the wavelength uniform and generates simple sinusoidal folding patterns. In contrast, large cortical growth rates  $G_c$  scale down subcortical growth. This generates higher compression in the cortex, which initiates the formation of secondary folds. According to the analytical estimates from Section 2, shorter critical wavelengths require a larger critical pressure before buckling is induced. For instance, in the bottom, left corner of Fig. 11, growth has not

yet generated sufficient compression to induce folding. If the cortex keeps on growing, this ellipse will buckle at a shorter wavelength than any of the other shown ellipses. The concurrence of slow growth rates and thick cortices prevents reaching a load high enough to initiate buckling.

## 6. Discussion

Despite its tremendous significance, little is known about the origin of cortical folding in the developing mammalian brain (Bayly et al., 2014). Two popular but competing hypotheses suggest that cortical folding originates either in the subcortex, driven by axonal tension (Van Essen, 1997), or in the cortex, driven by differential growth (Richman et al., 1975). Here we have combined both hypotheses into a bilayered material model for cortical folding, in which we represent the cortex as a morphogenetically growing outer layer (Holland et al., 2013), and the subcortex as a strain-driven growing inner core (Budday et al., 2014).

To gain first insight into these competing mechanisms (Bayly et al., 2013), we have established analytical estimates for the critical time, pressure, and wavelength at the onset of folding by modeling cortical folding by means of the instability problem of a confined, layered medium under growth-induced compression (Biot, 1957). We have shown that the critical wavelength  $\lambda^{\text{crit}}$ , the distance between two neighboring gyri, is directly proportional to the cortical thickness,  $\lambda^{\text{crit}} \propto t_c$ , proportional to the third root of the cortical-to-subcortical stiffness ratio,  $\lambda^{\text{crit}} \propto \sqrt[3]{E_c/E_s}$ , and proportional to the third root of the subcortical growth rate,  $\lambda^{\text{crit}} \propto \sqrt[3]{(G+G_s)/G}$ .

To explore the evolution of surface morphologies beyond the onset of folding, we have proposed a continuum model for finite growth, which we have solved computationally within a nonlinear finite element setting (Ambrosi et al., 2011). In regular rectangular geometries, we had to apply a small perturbation to trigger the formation of instabilities (Papastavrou et al., 2013). In agreement with the literature (Cao and Hutchinson, 2012), we observed that the computationally predicted surface morphology was relatively insensitive to the imposed mode of perturbation. In elliptic geometries, the heterogeneity in curvature was sufficient to initiate folding (Eskandari et al., 2013). The instability originated at the center of the long axis and then spread symmetrically outward.

We have systematically varied cortical thickness, stiffness, and growth and predicted folding patterns that were in excellent agreement with our analytical estimates. As expected, our computational model predicted a much wider variety of surface morphologies than the analytical solutions. In some cases, it even predicted the formation of secondary folds (Cao and Hutchinson, 2012). In general, folding patterns deviated from the symmetric sinusoidal ansatz towards morphologies with larger gyri and smaller sulci. This asymmetry reflects the impact of chronic axon elongation on gyral regions with positive stretch (Bray, 1984), which induces subcortical growth. As a natural consequence, the subcortical growth multiplier  $\vartheta$  displays significant regional variations with maxima of  $\vartheta > 2.0$  in the gyral centers and minima of  $\vartheta = 1.0$  indicating no growth at the sulcal base. This confirms that analytical modeling can provide valuable first insight into regular folding patterns (Biot, 1957), but computational modeling is mandatory to explore irregular brain surface morphologies (Budday et al., 2014).

### 6.1. Sensitivity of surface morphology with respect to cortical thickness

Of all parameters, our model seems to be most sensitive to variations in cortical thickness. Our simulations suggest that the intersulcal distance increases linearly with increasing cortical thickness (Biot, 1937). A considerably thickened cortex can even suppress the formation of folds entirely (Raybaud and Widjaja, 2011). This tendency is consistent with clinical pictures of diseased human brains: Lissencephaly, a malformation with a markedly thickened cortex, is characterized by a smooth brain surface (Landrieu et al., 1998); Polymicrogyria, a malformation with a regionally thinned cortex, is characterized by a highly convoluted brain surfaces with many small and superficial folds (Tortori-Donati et al., 2005). Thin cortices and decreased gyrification are associated with epilepsy, attention deficit hyperactivity disorder, dementia, mental retardation, and dyslexia; thick cortices and increased gyrification are associated with Williams syndrome, autism, and schizophrenia (Zilles et al., 2013). We conclude that the cortical thickness directly influences the gyral wavelength and is a key parameter to control surface morphology and primary folding.

### 6.2. Sensitivity of surface morphology with respect to stiffness ratio

The stiffness ratio between cortex and subcortex has a similar effect as the cortical thickness, however, only when scaled by its third root. Controlling surface morphology through the stiffness ratio has been discussed intensely in the materials sciences community (Cai et al., 2011), where thin stiff films on compliant substrates with stiffness ratios of up to four orders of magnitude play a major role (Audoly and Boudaoud, 2008). As the cortex with its neuronal cell bodies and synapses is much denser packed than the subcortex with its myelinated axons, it is intuitive that it may have a larger mechanical stiffness. Yet, experiments have shown that the cortical stiffness is less than an order of magnitude larger than the subcortical stiffness (vanDommelen et al.,). Some studies only found a stiffness difference of 50% (Christ et al., 2010). This has, in fact, been the major criticism of the first mechanical model for cortical folding based on the hypothesis of differential growth (Richman et al., 1975). We conclude that the stiffness ratio may influence surface morphology, but because of its small variation, it cannot be the single main driving force to explain cortical folding and morphological abnormalities.

### 6.3. Sensitivity of surface morphology with respect to growth ratio

Of all parameters, the growth ratio between cortex and subcortex seems to be the least well understood. Yet, it is probably the most important parameter to control the formation of secondary folds (Zang et al., 2012). In the continuum model, cortical and subcortical growth are introduced constitutively through the kinetics of growth in Eqs. (24) and (25). Eventually, we hope to tie these equations to cellular mechanisms such as axon elongation (Bray, 1984). In the analytical model, we have made a critical assumption to evaluate the relation between the critical wavelength, the time constant of growth, and the subcortical growth rate, namely that  $G = 1/t^{\text{crit}}$  (Bayly et al., 2013). At this point, this is a plain assumption, yet it provides some insight into the two extreme cases of abnormally slowly and abnormally fast growing cortices. Abnormally slowly growing cortices create an almost fluid-like behavior of the subcortex: axons are capable of responding almost instantaneously to growth-induced subcortical deformation and, in extreme cases, folding is suppressed entirely. Abnormally fast growing cortices create an elastic solid-like behavior of the subcortex: axons are incapable of responding to stretch, the pressure in the cortical layer raises quickly, and provokes the formation of secondary folds (Li et al., 2012). In the human brain, for example, primary folding begins at 22 weeks gestation and secondary folding takes place between weeks 25 and 30 (Raybaud and Widjaja, 2011). In the materials science community, these two types of folds are associated with kinematically induced instabilities, controlled by thickness and stiffness, and dynamically induced instabilities, controlled by growth rates (Huang, 2005). The interplay of kinematic and dynamic instabilities generates a wide variety of surface morphologies, in which secondary folding serves as a mechanism to release large compressive stresses in the outer layer (Cao and Hutchinson, 2012). We conclude that the growth ratio is a key parameter to control irregular surface morphologies and secondary folding.

### 6.4. Mechanical modeling explains surface morphologies of mammalian brains

From the explanted mammalian brains in Fig. 2, we conclude that brain size increases with increasing animal size (Hofman, 1989) from 140 g in sheep via 180 g in pigs to 450 g in cows (Nieuwenhuys et al., 1997). Yet, the average cortical thickness in the frontal coronal sections in Fig. 2 varies only marginally from 0.23 cm in the sheep via 0.22 cm in the pig to 0.22 cm in the cow brain. This is in line with the common understanding that the average cortical thickness varies marginally across mammalian species and is independent of brain size (Roth and Dicke, 2005). Similarly, the average gyral wavelength in Fig. 2 varies marginally from 0.61 cm in the sheep via 0.53 cm in the pig to 0.90 cm in the cow brain. According to our model, increasing the brain size at a constant cortical thickness does not affect the absolute gyral wavelength; yet, it increases the relative gyral wavelength when scaled by brain size. This is in agreement with a recent review, which reported the gyrification index, the ratio between the total brain surface area and the exposed surface area, to be 1.94 in sheep and 2.18 in pig (Zilles et al., 2013). Our model can thus explain why the surface-to-volume ratio of mammalian brains in Fig. 1 increases disproportionately faster than predicted by isometric scaling and why the degree of gyrification tends to increase with brain size.

### 6.5. Limitations

Both our analytical and our computational model provide valuable insight into the development of the mammalian brain. Yet, they have a few limitations, which could be addressed to make the models more realistic.

First, in our current model, we have neglected the geometric constraint by the skull. Our results indicate that the skull is not necessary to trigger gyrification; yet, it might be an important regulator of cortical folding (Nie et al., 2010). In our model, folding is constrained exclusively by the subcortical layer underneath the growing cortex. Adding a stiff skull above the growing cortex would certainly influence the final folding pattern, for example, by flattening out the gyral ridges. Yet, the impact if the skull on the initial gyral wavelength at the onset of folding might be rather minor (Bayly et al., 2013).

Second, here, we have assumed the constitutive behavior as quasi-incompressible with a Poisson's ratio of  $\nu = 0.458$  in the linear regime (Soza et al., 2005). Other studies suggest that brain tissue is nearly incompressible with  $\nu = 0.496$  (Franceschini, 2006) or entirely incompressible (Rashid et al., 2012, 2014). Our analytical model in Section 2 is generally valid for both compressible and incompressible materials. Our continuum model in Section 3 would require a different strain energy function in Eq. (20) to capture incompressibility exactly. Imposing incompressibility in the computational model in Section 4 would require additional modifications both on the constitutive level and on the element level, since the overall response would alternate between compressible during growth and incompressible during purely elastic phases (Rausch and Kuhl, 2014; Schmid et al., 2012).

Third, within this study, we have simplified the elastic response of the brain as Neo Hookean isotropic (Soza et al., 2005). Although the microstructure of both cortex and subcortex is clearly anisotropic, their anisotropic material behavior remains poorly characterized. The microstructure of the cortex is relatively regular and closely correlated with the radial direction  $\mathbf{r}_0$ , which defines the orientation of the cortical columns (Rakic, 1988). The microstructure of the subcortex is rather irregular and closely correlated with the axon orientation  $\mathbf{a}_0$ , which needs to be identified through diffusion tensor imaging (Mori and Zhang, 2006) or other novel imaging techniques (Chung and Deisseroth, 2013). Detailed measurements of the cortical stiffness, along and perpendicular to the cortical columns, supplemented by measurements of the subcortical stiffness, along and perpendicular to the axon orientation, would be tremendously valuable. To improve the elastic module of our model,

we are currently performing a series of nano-indentation tests (Zhang et al., 2010) to characterize cortical and subcortical stiffnesses, the degree of cortical and subcortical anisotropy, and the stiffness variation across different species.

Fourth, we have not only simplified the elastic behavior but also the growth response as isotropy. For cortical growth, we are currently working on replacing the isotropic growth tensor,  $\mathbf{F}^g = \vartheta \mathbf{I}$ , in Eq. (18) by an anisotropic growth tensor,  $\mathbf{F}^g = \vartheta^\perp \mathbf{I} + [\vartheta^\parallel - \vartheta^\perp] \mathbf{r}_0 \otimes \mathbf{r}_0$ , where  $\mathbf{r}_0$  characterizes the radial direction (Rausch and Kuhl, 2014). In this setup, the radial growth multiplier  $\vartheta^\parallel$  characterizes cortical thickening along radial direction (Göktepe et al., 2010), and the surface growth multiplier  $\vartheta^\perp$  characterizes area growth perpendicular to it (Buganza Tepole et al., 2011). This allows us to replace the single phenomenological evolution of cortical growth,  $\vartheta = G_c$ , in Eq. (24) by two independent equations for cortical thickening and surface growth. We can then mechanically link surface growth,  $\vartheta^\perp = G_c^\perp$ , to the symmetric cell division of progenitor cells into two new progenitor cells, and thickness growth,  $\vartheta^\parallel = G_c^\parallel$  to the asymmetric cell division into a progenitor cell and a neuron (Roth and Dicke, 2005). For subcortical growth, we could replace the growth tensor  $\mathbf{F}^s = \vartheta \mathbf{I}$ , in Eq. (18) by an anisotropic growth tensor,  $\mathbf{F}^s = \mathbf{I} + [\vartheta^\parallel - 1] \mathbf{a}_0 \otimes \mathbf{a}_0$ , where  $\mathbf{a}_0$  characterizes the axon orientation (Zöllner et al., 2012). The growth multiplier  $\vartheta^\parallel$  characterizes the chronic axon elongation in response to overstretch (Denneril et al., 1989). We could then replace elastic volume change ( $J^e - J^0$ ) as the driving force for subcortical growth,  $\vartheta^\parallel = G_c \langle J^e - J^0 \rangle$ , in Eq. (25) by the elastic axonal stretch  $\langle \lambda^e - \lambda^0 \rangle$  with  $\lambda^e = [\mathbf{a}_0 \cdot \mathbf{F}^t \cdot \mathbf{F} \cdot \mathbf{a}_0]^{1/2}$ , to correlate the model parameters to experimentally measured axon elongation rates (Bray, 1984).

Finally, growth is neither homogeneous in space nor constant in time. To functionally correlate cellular and molecular events to cortical and subcortical growth (Knutsen et al., 2013), we could turn different growth rates on and off to better represent the sequence of events during gyrogenesis, including neuronal proliferation, differentiation, apoptosis, dendrogenesis, synapsogenesis, glial proliferation, lamination, and cellular rearrangement (Raybaud and Widjaja, 2011).

## 7. Concluding remarks

Mechanical modeling of brain development can explain variations in surface morphology of the mammalian brain. Variations in cortical and subcortical thickness, stiffness, or growth can generate variations in pattern formation. A thinner, softer, or slower growing layer of gray matter generally enhances cortical folding and reduces the gyral wavelength. A thicker, stiffer, or faster growing layer of gray matter reduces cortical folding and increases the gyral wavelength. Larger mammals tend to have larger brains, but similar cortical thicknesses. Our model predicts that the absolute gyral wavelength in mammals is almost constant across different species, while the relative gyral wavelength increases with brain size. This explains why the surface-to-volume ratio of mammalian brains increases disproportionately faster than predicted by isometric scaling. Our model can also explain the pathological malformations of polymicrogyria, associated with a thin and overly convoluted cortex, and lissencephaly, associated with a thick and poorly convoluted cortex. Understanding the mechanisms of cortical folding during brain development may have direct implications on the diagnostics of neurological disorders, including severe retardation, epilepsy, schizophrenia, and autism.

## Acknowledgments

This study was supported by the German National Science Foundation grant STE 544/50-1 to Silvia Budday and Paul Steinmann, by the National Science Foundation CAREER award CMII 0952021, by the National Science Foundation INSPIRE grant 1233054, and by the National Institutes of Health Grant U54GM072970 to Ellen Kuhl.

## References

- Allen, H.G., 1969. Analysis and Design of Structural Sandwich Panels. Pergamon Press, Oxford.
- Ambrosi, D., Mollica, F., 2002. On the mechanics of a growing tumor. *Int. J. Eng. Sci.* 40, 1297–1316.
- Ambrosi, D., Ateshian, G.A., Arruda, E.M., Cowin, S.C., Dumais, J., Goriely, A., Holzapfel, G.A., Humphrey, J.D., Kemkemer, R., Kuhl, E., Olberding, J.E., Taber, L.A., Garikipati, K., 2011. Perspectives on biological growth and remodeling. *J. Mech. Phys. Solids* 59, 863–883.
- Audoly, B., Boudaoud, A., 2008. Buckling of a stiff film bond to a compliant substrate—Part I: formulation, linear stability of cylindrical patterns, secondary bifurcations. *J. Mech. Phys. Solids* 56, 2401–2421.
- Audoly, B., Boudaoud, A., 2008. Buckling of a stiff film bond to a compliant substrate—Part II: a global scenario for the formation of herringbone pattern. *J. Mech. Phys. Solids* 56, 2422–2443.
- Bayly, P.V., Okamoto, R., Xu, G., Shi, Y., Taber, L.A., 2013. A cortical folding model incorporating stress-dependent growth explains gyral wavelengths and stress patterns in the developing brain. *Phys. Biol.* 10, 016005.
- Bayly, P.V., Taber, L.A., Kroenke, C.D., 2014. Mechanical forces in cerebral cortical folding: a review of measurements and models. *J. Mech. Behav. Biomed. Mater.* 29, 568–581.
- BenAmar, M., Goriely, A., 2005. Growth and instability in elastic tissues. *J. Mech. Phys. Solids* 53, 2284–2319.
- Biot, M.A., 1937. Bending of an infinite beam on an elastic foundation. *J. Appl. Mech.* 59, A1–A7.
- Biot, M.A., 1957. Folding instability of a layered viscoelastic medium under compression. *Proc. R. Soc. London A* 242, 444–454.
- Bray, D., 1984. Axonal growth in response to experimentally applied mechanical tension. *Dev. Biol.* 102, 379–389.
- Budday, S., Raybaud, C., Kuhl, E., 2014. A mechanical model predicts morphological abnormalities in the developing human brain. *Sci. Reports* 4, 5644.
- Buganza Tepole, A., Ploch, C.J., Wong, J., Gosain, A.K., Kuhl, E., 2011. Growing skin—a computational model for skin expansion in reconstructive surgery. *J. Mech. Phys. Solids* 59, 2177–2190.
- Cai, S., Breid, D., Crosby, A.J., Suo, Z., Hutchinson, J.W., 2011. Periodic patterns and energy states of buckled thin films on compliant substrates. *J. Mech. Phys. Solids* 59, 1094–1114.
- Cao, Y., Hutchinson, J.W., 2012. From wrinkles to creases in elastomers: the instability and imperfection-sensitivity of wrinkling. *Proc. R. Soc. A* 468, 94–115.
- Cao, Y., Hutchinson, J.W., 2012. Wrinkling phenomena in Neo-Hookean film/substrate bilayers. *J. Appl. Mech.* 79, 031019.1–031019.9.

- Chada, S., Lamoureux, P., Buxbaum, R.E., Heidemann, S.R., 1997. Cytomechanics of neurite outgrowth from chick brain neurons. *J. Cell Sci.* 110, 1179–1186.
- Christ, A.F., Franze, K., Gautier, H., Moshayedi, P., Fawcett, J., Franklin, R.J.M., Karadottir, R.T., Guck, J., 2010. Mechanical differences between white and gray matter in the rat cerebellum measured by scanning force microscopy. *J. Biomech.* 43, 2986–2992.
- Chung, K., Deisseroth, K., 2013. CLARITY for mapping the nervous system. *Nat. Methods* 10, 508–513.
- Dennerli, T.J., Lamoureux, P., Buxbaum, R.E., Heidemann, S.R., 1989. The cyto mechanics of axonal elongation and retraction. *J. Cell Biol.* 109, 3073–3083.
- Dervaux, J., Ciarletta, P., Ben Amar, M., 2009. Morphogenesis of thin hyperelastic plates: a constitutive theory of biological growth in the Föppl–von Kármán limit. *J. Mech. Phys. Solids* 57, 458–471.
- Eskandari, M., Pfaller, M.R., Kuhl, E., 2013. On the role of mechanics in chronic lung disease. *Materials* 6, 5639–5658.
- Föppl, A., 1907. *Vorlesungen über technische Mechanik*, vol. 5. B.G. Teubner, Leipzig.
- Franceschini, G., 2006. *The Mechanics of Human Brain Tissue. Modelling, Preservation and Control of Materials and Structures*. Ph.D. Thesis. University of Trento.
- Franceschini, G., Bigoni, D., Regitnig, P., Holzappel, G.A., 2006. Brain tissue deforms similarly to filled elastomers and follows consolidation theory. *J. Mech. Phys. Solids* 54, 2592–2620.
- Garikipati, K., 2009. The kinematics of biological growth. *Appl. Mech. Rev.* 62, 030801.1–030801.7.
- Geschwind, D.H., Rakic, P., 2013. Cortical evolution: Judge the brain by its cover. *Neuron* 80, 633–647.
- Göktepe, S., Abilez, O.J., Kuhl, E., 2010. A generic approach towards finite growth with examples of athlete's heart, cardiac dilation, and cardiac wall thickening. *J. Mech. Phys. Solids* 58, 1661–1680.
- Herculano-Houzel, S., 2009. The human brain in numbers: a linearly scaled-up primate brain. *Front. Hum. Neurosci.* 3, 31.1–31.11.
- Hatten, M.E., 1999. Central nervous system neuronal migration. *Annu. Rev. Neurosci.* 22, 2511–2539.
- Hofman, M.A., 1989. On the evolution and geometry of the brain in mammals. *Prog. Neurobiol.* 32, 137–158.
- Holland, M.A., Kosmata, T., Goriely, A., Kuhl, E., 2013. On the mechanics of thin films and growing surfaces. *Math. Mech. Solids* 18, 561–575.
- Huang, R., 2005. Kinetic wrinkling of an elastic film on a viscoelastic substrate. *J. Mech. Phys. Solids* 53, 63–89.
- Knutsen, A.K., Kroenke, C.D., Chang, Y.V., Taber, L.A., Bayly, P.V., 2013. Spatial and temporal variations of cortical growth during gyrogenesis in the developing ferret brain. *Cereb. Cortex* 23, 488–498.
- Kuhl, E., 2014. Growing matter—a review of growth in living systems. *J. Mech. Behav. Biomed. Mater.* 29, 529–543.
- Landrieu, P., Husson, B., Pariente, D., Lacroix, C., 1998. MRI-neuropathological correlations in type 1 lissencephaly. *Neuroradiology* 40, 173–176.
- Le Gros Clark, W.E., 1945. Deformation patterns in the cerebral cortex. In: Le Gros Clark, W.E., Medawar, P.B. (Eds.), *Essays on Growth and Form*. Oxford University Press, London, pp. 1–22.
- Li, B., Cao, Y.P., Feng, X.Q., Gao, H., 2011. Surface wrinkling of mucosa induced by volumetric growth: theory, simulation and experiment. *J. Mech. Phys. Solids* 59, 758–774.
- Li, B., Cao, Y.P., Feng, X.Q., Gao, H., 2012. Mechanics of morphological instabilities and surface wrinkling in soft materials: a review. *Soft Matter* 8, 5728–5745.
- Lubarda, V.A., 2004. Constitutive theories based on the multiplicative decomposition of deformation gradient: thermoelasticity, elastoplasticity, and biomechanics. *Appl. Mech. Rev.* 57, 95–108.
- Menzel, A., Kuhl, E., 2012. Frontiers in growth and remodeling. *Mech. Res. Commun.* 42, 1–14.
- Mori, S., Zhang, J., 2006. Principles of diffusion tensor imaging and its applications to basic neuroscience research. *Neuron* 51, 527–539.
- Moulton, D.E., Goriely, A., 2011. Circumferential buckling instability of a growing cylindrical tube. *J. Mech. Phys. Solids* 59, 525–537.
- Nie, J., Guo, L., Faraco, C., Miller, L.S., Liu, T., 2010. A computational model of cerebral cortex folding. *J. Theor. Biol.* 264, 467–478.
- Nieuwenhuys, R., Donkelaar, H.J., Nicholson, C., 1997. *The Central Nervous System of Vertebrates*. Springer-Verlag, Berlin.
- Papastavrou, A., Steinmann, P., Kuhl, E., 2013. On the mechanics of continua with boundary energies and growing surfaces. *J. Mech. Phys. Solids* 61, 1446–1463.
- Rakic, P., 1988. Specification of cerebral cortical areas. *Science* 241, 170–176.
- Rashid, B., Destrade, M., Gilchrist, M.D., 2012. Mechanical characterization of brain tissue in compression at dynamic strain rates. *J. Mech. Behav. Biomed. Mater.* 10, 23–38.
- Rashid, B., Destrade, M., Gilchrist, M.D., 2014. Mechanical characterization of brain tissue in tension at dynamic strain rates. *J. Mech. Behav. Biomed. Mater.* 33, 43–54.
- Rausch, M.K., Kuhl, E., 2014. On the mechanics of growing thin biological membranes. *J. Mech. Phys. Solids* 63, 128–140.
- Raybaud, C., Widjaja, E., 2011. Development and dysgenesis of the cerebral cortex: malformations of cortical development. *Neuroimaging Clin. N. Am.* 21, 483–543.
- Richman, D.P., Stewart, R.M., Hutchinson, J.W., Caviness, V.S., 1975. Mechanical model of brain convolitional development. *Science* 189, 18–21.
- Rodriguez, E.K., Hoger, A., McCulloch, A.D., 1994. Stress-dependent finite growth in soft elastic tissues. *J. Biomech.* 27, 455–467.
- Roth, G., Dicke, U., 2005. Evolution of the brain and intelligence. *Trends Cogn. Sci.* 9, 250–257.
- Ronan, L., Voets, N., Rua, C., Alexander-Block, A., Hough, M., Mackay, C., Crow, T.J., James, A., Giedd, J.N., Fletcher, P.C., 2014. Differential tangential expansion as a mechanism for cortical gyrification. *Cereb. Cortex* 24, 2219–2228.
- Schmid, H., Pauli, L., Paulus, A., Kuhl, E., Itskov, M., 2012. Consistent formulation of the growth process at the kinematic and constitutive level for soft tissues composed of multiple constituents. *Comput. Methods Biomech. Biomed. Engin.* 15, 547–561.
- Schwartzkroin, P.A., Walsh, C.A., 2000. Cortical malformations and epilepsy. *Ment. Retard. Dev. Disabil. Res. Rev.* 6, 268–280.
- Soza, G., Grosso, R., Nimsky, C., Hastreiter, P., Fahlbusch, R., Greiner, G., 2005. Determination of the elastic parameters of brain tissue with combined simulation and registration. *Int. J. Med. Robot. Comp. Assist. Surg.* 1, 87–95.
- Sun, T., Hevner, R.F., 2014. Growth and folding of the mammalian cerebral cortex: from molecules to malformations. *Nat. Rev. Neurosci.* 15, 217–232.
- Tortori-Donati, P., Rossi, A., Biancheri, R., 2005. Brain malformations. In: *Pediatric Neuroradiology*. Springer, Berlin, Heidelberg, pp. 71–198.
- van Dommelen, J.A.W., vanderSande, T.P.J., Hrapko, M., Peters, G.W.M., Mechanical properties of brain tissue by indentation: interregional variation. *J. Mech. Behav. Biomed. Mater.* 3, 158–166.
- Van Essen, D.C., 1997. A tension-based theory of morphogenesis and compact wiring in the central nervous system. *Nature* 385, 313–318.
- von Kármán, T., 1910. Festigkeitsproblem im Maschinenbau. *Encyklopädie der Mathematischen Wissenschaften*, vol. 4, pp. 311–385.
- Xu, G., Knutsen, A.K., Dikranian, K., Kroenke, C.D., Bayly, P.V., Taber, L.A., 2010. Axons pull on the brain, but tension does not drive cortical folding. *J. Biomech. Eng.* 132, 071013.
- Welker, W., Johnson, I.J., Noe, A., Comparative mammalian brain collections. (<http://brainmuseum.org>).
- Welker, W., 1990. Why does cerebral cortex fissure and fold? A review of determinants of gyri and sulci. In: Jones, E.G., Peters, A. (Eds.), *Cerebral Cortex*, vol. 8B. Springer Science+Business Media, New York.
- Zang, J., Zhao, X., Cao, Y., Hutchinson, J.W., 2012. Localized ridge wrinkling of stiff films on compliant substrates. *J. Mech. Phys. Solids* 60, 1265–1279.
- Zhang, J., Michalenko, M.M., Kuhl, E., Ovaert, T.C., 2010. Characterization of indentation response and stiffness reduction of bone using a continuum damage model. *J. Mech. Behav. Biomed. Mater.* 3, 189–202.
- Zilles, K., Armstrong, E., Schleicher, A., Kretschmann, H.J., 1988. The human pattern of gyrification in the cerebral cortex. *Anat. Embryol.* 179, 173–179.
- Zilles, K., Palomero-Gallagher, N., Amunts, K., 2013. Development of cortical folding during evolution and ontogeny. *Trends Neurosci.* 36, 275–284.
- Zöllner, A.M., Abilez, O.J., Böl, M., Kuhl, E., 2012. Stretching skeletal muscle—chronic muscle lengthening through sarcomerogenesis. *PLoS One* 7 (10), e45661.